

RESEARCH ARTICLE

WILEY

Transient computational homogenization of heterogeneous poroelastic media with local resonances

Renan Liupekevicius¹ | Johannes A. W. van Dommelen² | Marc G. D. Geers³ |
Varvara G. Kouznetsova¹

Mechanical Engineering, Eindhoven
University of Technology, The Netherlands

Correspondence

Varvara G. Kouznetsova, Mechanical
Engineering, Eindhoven University of
Technology, The Netherlands.
Email: v.g.kouznetsova@tue.nl

Funding information

Nederlandse Organisatie voor
Wetenschappelijk Onderzoek

Abstract

A computational homogenization framework is proposed for solving transient wave propagation in the linear regime in heterogeneous poroelastic media that may exhibit local resonances due to microstructural heterogeneities. The microscale fluid-structure interaction problem and the macroscale are coupled through an extended version of the Hill-Mandel principle, leading to a variationally consistent averaging scheme of the microscale fields. The effective macroscopic constitutive relations are obtained by expressing the microscale problem with a reduced-order model that contains the longwave basis and the so-called local resonance basis, yielding the closed-form expressions for the homogenized material properties. The resulting macroscopic model is an enriched porous continuum with internal variables that represent the microscale dynamics at the macroscale, whereby the Biot model is recovered as a special case. Numerical examples demonstrate the framework's validity in modeling wave transmission through a porous layer.

KEYWORDS

computational homogenization, micromorphic enriched continuum, poroelasticity, resonant microstructure

1 | INTRODUCTION

The homogenization of coupled phenomena in heterogeneous media is a challenge that becomes attractive for fast simulations at engineering scales. The method proposed in this article addresses the development of less computationally demanding models that accurately describe the transient wave propagation in heterogeneous materials. The appropriate description of the wave propagation problem attracts attention for applications in geomechanics, biological tissues, sound-absorbing materials, and the new class of emerging acoustic metamaterials. Locally resonant acoustic metamaterials (LRAMs) are engineered materials that exhibit interesting macroscopic properties for wave control such as bandgaps, that is, a gap in the wave spectrum, where for certain frequencies, waves cannot propagate due to the

This article is dedicated to Robert L. Taylor on the occasion of his 90th birthday. Throughout the decades, the work of Bob Taylor has been foundational for the development of finite element formulations for fluids and solids, including his more recent interest in the multiscale methods, which are the three focal points of the present contribution. With this contribution, we would like to honor his work and achievements for a sustained period of almost 60 years.

This is an open access article under the terms of the [Creative Commons Attribution](https://creativecommons.org/licenses/by/4.0/) License, which permits use, distribution and reproduction in any medium, provided the original work is properly cited.

© 2024 The Authors. *International Journal for Numerical Methods in Engineering* published by John Wiley & Sons Ltd.

microstructural dynamics. In this case, the account for microinertial effects is essential for proper macroscopic material modeling as discussed by Milton and Willis.¹ Therefore, for these challenging applications, a macroscopic model for porous structures should properly account for the underlying coupled processes and the microinertia.

When the underlying physics is known at a small scale, a macroscale effective behavior can be obtained with multiple approaches. Developing an appropriate transient macroscopic description for wave propagation in fluid-saturated deformable porous solids is challenging. The multiplicity originates from the rather different nature of the coupled equations of motion for each constituent that must span several time and length scales, and, eventually, account for irreversible processes and inertia at the pore scale.

1.1 | Homogenization neglecting microscale inertia

Neglecting the microscale inertia and focusing mainly on linear mechanics, it is indispensable to discuss the work of Biot² which belongs to the class of macroscopic models of deformable porous solids. Biot postulated the elastic and kinematic energy of the solid-fluid aggregate, leading to coupled macroscopic constitutive relations for each phase, successfully describing wave propagation in porous materials. Such purely macroscopic descriptions are, however, disconnected from the pore-scale physics, as pointed out in the survey of Serpieri et al.³ Mixture theory is a more foundational approach based on superimposed continua. For example, Bedford and Drumheller⁴ derived Biot's equation of motion solely from variational principles by introducing a volume fraction constraint into Hamilton's principle with the method of Lagrange multipliers. Mixture theory allows more elaborated types of interactions between immiscible mixtures such as two-phase fluids, see Bedford,⁵ for a comprehensive overview of the method.

The rigorous derivation of Biot's equations based on the microscale pore physics was carried out by Burridge and Keller⁶ using a two-scale asymptotic homogenization approach where the microscale problem is defined as a porous elastic solid saturated by a fluid governed by the linearized Navier-Stokes equations. Burridge's approach demonstrated the power of multiscale methods for, not only, deriving Biot's equation as a limit case for the fluid's dimensionless viscosity but also, as another limit, the equation of a viscoelastic solid. Using the Slattery averaging theorem and inspired by the work of Whitaker⁷ for deriving Darcy's law, Pride et al.⁸ derived Biot's equation of motion by directly averaging the governing equations of an elastic solid saturated by a fluid described by the linearized Navier-Stokes equations. These derivations underline the robustness of Biot's macroscopic description as a poroelastic continuum.

The representative volume element (RVE)-based methods, such as computational homogenization, which were extensively discussed in Geers et al.,^{9,10} prove to be versatile and capable of upscaling complex, nonlinear phenomena and evolving microstructures, originally developed neglecting microinertial effects. Using the separation of scales argument, it is reasonable to assume a steady-state condition at the microscale. The method is based on the Hill-Mandel principle, which, by a variationally consistent average of the virtual power, couples micro, and macroscales, essentially delivering a macroscopic continuum model. Despite, the steady state condition at the microscale, transient macroscopic problems can be solved, as pointed out by Matouš et al.,¹¹ simply by taking the volume average of the material property related to the transient term, for instance, the mass density. Özdemir et al.¹² implemented this idea for a macroscopic heat conduction problem where the heat storage is volume averaged. The transient analysis of porous materials using computational homogenization continued toward defining the heterogeneous RVE as a combination of a solid and a porous matrix, essentially assuming the Biot model at the microscopic level which in practice avoids direct modeling of the fluid phase. This was first done in the context of a transient consolidation problem by Larsson et al.¹³ and Su et al.,¹⁴ then, in a seismic wave propagation problem by Jänicke et al.^{15,16} and Quintal et al.¹⁷ where the macroscale was assumed as an equivalent viscoelastic solid. The so-called selective homogenization approach was used to eliminate the macroscopic fluid pressure. It is noteworthy that in the latter works, local Darcy flow occurs within the defined RVE, where the microscale transient term comes from the mass balance equation. Later on, a transient wave analysis incorporating the macroscopic fluid pressure¹⁸ was developed in a non-selective homogenization approach. Notably, in Jänicke et al.,^{16,18} the use of a proper orthogonal decomposition as a reduced basis greatly reduced the computational cost of the microscale time-dependent problem, yielding a set of evolving internal variables at the macroscale. Here, a similar reduced model approach will be considered using a spectral reduced basis. The computational homogenization approach, without macroscopic transient terms, was also applied to a rigid porous structure saturated by a Newtonian fluid, yielding a macroscopic Darcy flow by Sandsdröm et al.^{19,20} followed by incorporation of the solid displacement²¹ allowing to compute material properties of the solid skeleton predicted by the Biot theory. However, since in the latter work, the macroscopic analysis assumed steady-state conditions, the wave propagation problem could not be considered. Finally, in the work of Gao et al.,^{22,23}

a computational homogenization approach was presented using an extended version of the Hill-Mandel principle for an elastic porous solid saturated by a fluid governed by the linearized Navier-Stokes equation, leading to a macroscopic wave propagation equivalent to the Biot equations relying on a selective homogenization approach where the viscous stress redistribution is only allowed within the RVE. However, time-harmonicity was assumed for both scales leading to frequency-dependent material properties that limit the analysis of pulse excitations with a broad frequency content. For instance, to handle frequency-dependent material properties for conducting transient acoustic wave analysis, Fellah et al.²⁴ employs a fractional calculus approach that requires special numerical treatment, for example, for a finite element implementation. Other notable works include the hybrid homogenization approach of Perrot et al.²⁵ and Zielinski et al.²⁶ for upscaling frequency-dependent material properties based on RVE simulations neglecting microscale inertia.

1.2 | Homogenization including microscale inertia

Wave propagation in heterogeneous porous media may also involve phenomena where the pore scale dynamics, originating from the balance of linear momentum, play an important role in the effective macroscopic response. Bedford and Drumheller,²⁷ proposed a purely macroscopic model including microinertial effects added to Hamilton's principle as an extra kinematic descriptor and an energy associated with the expansion of gas bubbles. Several macroscopic modified Biot models accounting for resonating effects of bubbles in fluid-saturated porous solids have recently been proposed in the context of geomechanics applications.^{28–32} These macroscopic models can describe the dispersion of waves owing to the microscale dynamics and dissipation. Novel approaches based on pore-scale physics, for instance, by Venegas and Boutin,³³ use asymptotic homogenization accounting for resonances taking place in thin membranes in the pores.

The computational homogenization framework developed by Gao et al.²² was applied by Lewinska et al.^{34,35} to a locally resonant porous foam saturated by a dissipative fluid in the context of sound insulation. Despite being limited to frequency domain analysis, it was successful and capable of upscaling the microscale inertial contributions that are, essentially, embedded in the frequency-dependent homogenized material properties. Moreover, computational homogenization frameworks including the microscale inertial contribution for transient consolidation, by Khoei and Hajiabadi,³⁶ and transient wave propagation, by Wu et al.,³⁷ were carried out. However in these two works, the fluid phase was not explicitly modeled; instead, a porous matrix (Biot model) and a solid at the microscale are assumed.

In parallel to the developments for fluid-saturated porous materials, the microscale dynamics was incorporated in macroscale models for the computational homogenization of solid LRAMs, that is, metamaterials containing a resonator embedded in a stiff matrix. To accomplish this, a relaxed separation of scales was introduced where only the solid matrix is required to be in the longwave regime. Rigorous asymptotic homogenization was done by Auriault and Boutin³⁸ showing the presence of bandgaps and wave dispersion. The computational homogenization method was applied to LRAMs by Pham et al.,³⁹ employing the extended Hill-Mandel principle that enabled the upscaling of the microscale inertia contributions. This approach is capable of performing macroscale transient wave propagation analysis in linear and nonlinear regimes where the microscale dynamics cause highly dispersive wave propagation at the frequency of the bandgap.^{39,40} Within a similar approach, restricted to the linear regime, Sridhar et al.⁴¹ used a reduced spectral basis for describing the microscale dynamics, leading to a macroscale model with internal variables that describe the localized resonances. Sridhar's framework proved to be successful in describing both time-harmonic and transient wave propagation problems applied to different cases of solid LRAMs.^{42–44}

This article proposes a computational homogenization approach for transient wave propagation in saturated porous materials employing a reduced-order model for the microscale problem. A linear locally resonant elastic deformable porous solid saturated by an inviscid compressible fluid is selected for demonstrating the framework's capabilities of including the influence of the microdynamics on the macroscale wave propagation. The novel contributions of this work are:

- A porous macroscopic continuum description based on the computational homogenization approach that enables transient wave analyses in the time domain, unlike Gao et al.²² and Lewinska et al..^{34,35}
- The proposed multiscale method computes the homogenized material properties based on microstructural simulations leading to general, non-standard, constitutive relations, including the material properties predicted in the Biot model as a subset. It differs from Gao et al.²² where the macroscopic constitutive response was assumed according to the Biot model in the frequency domain. It also differs from Sandström et al.²¹ where the homogenized elastic material properties are computed in the longwave regime. Here, the inertial material properties are also determined.

- The microscale problem uses a model order reduction technique, leading to an efficient microscale problem unlike the fully resolved RVE.^{36,37,39,40} In this work, the microscale dynamics contribution is upscaled as an explicit set of internal variables.
- The microscale problem includes coupled fluid-structure interaction, while the work of Sridhar et al.⁴¹ included only a solid. Moreover, the explicit description of the fluid phase differs from Jänicke et al.¹⁵ where the fluid was modeled implicitly defining a porous matrix at the microscale, with the transient terms exclusively obtained from the mass balance equation.

The article is organized as follows: first, the governing equations of a fluid-structure interaction problem are defined. The computational homogenization framework is presented by coupling macro and microscales in a variationally consistent manner based on the extended Hill-Mandel condition. Next, a reduced-order model is proposed to simplify the microscale dynamics effects that are upscaled as internal variables. Finally, numerical examples show the comparison between the full-field response and the response of the proposed homogenized continuum where the effective Biot model is recovered when microinertia is neglected.

For clarity, the mathematical notations are defined in this paragraph. The mathematical objects used are scalars (0th order tensor), vectors (1st-order tensor), 2nd-order tensors, 3rd-order tensors, and 4th-order tensors and are represented as $a, \vec{a}, \mathbf{A}, {}^3\mathbf{A}$ and ${}^4\mathbf{A}$, respectively. The inner product and double-inner product are represented, respectively, as $\mathbf{A} \cdot \mathbf{B} = A_{ij}B_{jk}\vec{e}_i \otimes \vec{e}_k$, and $\mathbf{A} : \mathbf{B} = A_{ij}B_{ji}$, where $\{\vec{e}_1, \vec{e}_2, \vec{e}_3\}$ represent the Cartesian basis. The dyadic product between tensors is denoted as $\vec{a} \otimes \vec{b} = a_i a_j \vec{e}_i \otimes \vec{e}_j$, except for the gradient where it is omitted, that is, $\vec{\nabla} \vec{a} = \frac{\partial a_i}{\partial x_i} \vec{e}_i \otimes \vec{e}_j$. The 2nd- and 4th-order unit tensors are $\mathbf{I} = \delta_{ij} \vec{e}_i \otimes \vec{e}_j$ and ${}^4\mathbf{I} = \delta_{ij} \delta_{jk} \vec{e}_i \otimes \vec{e}_j \otimes \vec{e}_k \otimes \vec{e}_l$, respectively, where δ_{ij} is the Kronecker delta. The inverse and transpose of a 2nd-order tensor are denoted by $(\bullet)^{-1}$ and $(\bullet)^T$, respectively, and for 3rd- and 4th-order tensor the left and right transpose are denoted as $(\bullet)^{LT}$ and $(\bullet)^{RT}$, respectively. The notation (\bullet) and $(\underline{\bullet})$ are used for column and matrix assemblies, respectively. The entries of columns and matrices may be scalars, vectors, tensors, or combinations thereof. The inverse of a matrix is denoted by $(\underline{\bullet})^{-1}$. The transpose of a column and a matrix are denoted $(\bullet)^T$ and $(\underline{\bullet})^T$, respectively. Macroscopic quantities are identified with the subscript “M”, while microscopic quantities do not have such an index.

For simplicity of the derivations, *hybrid* columns and matrices are defined when the entries are a combination of scalars and vectors (for example, displacement and pressure). When scalars and vectors are assembled in the *same* column or matrix they are denoted as $\underline{\underline{a}}$ and $\underline{\underline{a}}$, respectively as

$$\underline{\underline{a}} = \begin{bmatrix} \vec{a} \\ a \end{bmatrix} \quad \text{and} \quad \underline{\underline{a}} = \begin{bmatrix} \underline{\underline{a}}^{(1)} & \dots & \underline{\underline{a}}^{(j)} & \dots \end{bmatrix} = \begin{bmatrix} \vec{a} \\ a \end{bmatrix}. \quad (1)$$

Similarly, when scalars, vectors, and 2nd-order tensors are assembled in the *same* matrix it is denoted a *hybrid* matrix $\underline{\underline{a}}$

$$\underline{\underline{a}} = \begin{bmatrix} \underline{\underline{A}} & \vec{a} \\ \vec{a} & a \end{bmatrix} \quad (2)$$

that can operate on a column $\underline{\underline{b}}$ such that $\underline{\underline{c}} = \underline{\underline{a}} \underline{\underline{b}}$. For this reason, the inner product “dot” is written together with the appropriate submatrices of the *hybrid* matrix.

2 | COMPUTATIONAL HOMOGENIZATION FRAMEWORK

2.1 | Governing equations in each phase

The dynamic response of a poroelastic material consists of a coupled fluid-structure interaction problem as depicted in Figure 1A.

A linear set of partial differential equations governs the coupled fluid-solid aggregate dynamics where each phase satisfies its respective equations of motion. The solid-phase balance of linear momentum and the fluid-phase wave equation of a compressible ideal fluid with a quiescent background are given by

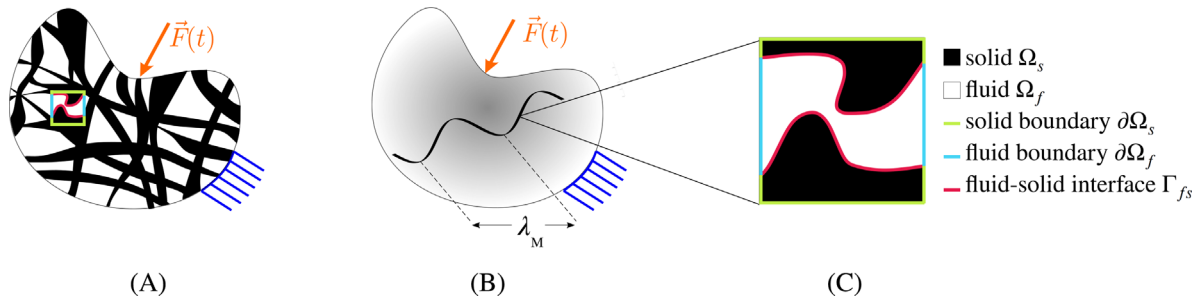


FIGURE 1 (A) Full-field problem. An elastic solid domain Ω_s^{FULL} (black) and a compressible ideal fluid domain Ω_f^{FULL} (white) with a fluid-solid interface $\Gamma_{fs}^{\text{FULL}}$ composing a porous domain subjected to boundary conditions and time-dependent loading. (B) Equivalent macroscopic domain Ω_M subjected to boundary conditions and time-dependent loading with a representative macroscopic wavelength λ_M . (C) Representative volume element (RVE), with the definition of microscopic solid and fluid domains Ω_s and Ω_f enclosed by their respective surfaces $\partial\Omega_s \cup \Gamma_{fs}$ and $\partial\Omega_f \cup \Gamma_{fs}$ with the color coding given in the legend.

$$\begin{aligned} \dot{\vec{\pi}}(\vec{x}, t) - \vec{\nabla} \cdot \vec{\sigma}^T(\vec{x}, t) &= \vec{0} \quad \text{in } \Omega_s^{\text{FULL}} \times [t_1, t_2] \\ -\dot{\epsilon}(\vec{x}, t) + \vec{\nabla} \cdot \ddot{\vec{U}}(\vec{x}, t) &= 0 \quad \text{in } \Omega_f^{\text{FULL}} \times [t_1, t_2], \end{aligned} \quad (3)$$

where the solid linear momentum $\vec{\pi}$ is the conserved field with the corresponding flux given by the solid stress $\vec{\sigma}$. Similarly, the wave equation for the fluid is written as the conservation of volumetric strain rate ϵ with the corresponding flux given by the acceleration of the fluid $\ddot{\vec{U}}$. See Appendix A for a more elaborate description of the problem assumptions and other equivalent forms of the balance equations. The governing Equation (3) are expressed here in the conservation form, that is, defining the rates of the conserved fields and their fluxes, which is a convenient format for the subsequent derivations of the effective macroscopic constitutive relations, developed in Section 2.4. Commonly, the primary unknown fields are the solid displacement $\vec{u}(\vec{x}, t)$ and the fluid pressure disturbance $p(\vec{x}, t)$ around an equilibrium state (background pressure). The constitutive relations are

$$\begin{aligned} \vec{\pi}(\vec{x}, t) &= \rho_s \dot{\vec{u}}(\vec{x}, t), & \epsilon(\vec{x}, t) &= -\frac{1}{K_f} p(\vec{x}, t), \\ \vec{\sigma}(\vec{x}, t) &= {}^4\mathbf{C}_s : \vec{\nabla} \vec{u}(\vec{x}, t), & \ddot{\vec{U}}(\vec{x}, t) &= -\frac{1}{\rho_f} \vec{\nabla} p(\vec{x}, t), \end{aligned} \quad (4)$$

where ρ_s and ${}^4\mathbf{C}_s = K_s \mathbf{II} + G_s \left(({}^4\mathbf{I} + {}^4\mathbf{I}^{\text{RT}}) - \frac{2}{3} \mathbf{II} \right)$ are, respectively, the solid mass density and isotropic elastic stiffness tensor; ρ_f and K_f are the fluid mass density and bulk modulus at an equilibrium state. Note that in Equation (4), the commonly used strain tensor $\frac{1}{2}(\vec{\nabla} \vec{u}(\vec{x}, t) + (\vec{\nabla} \vec{u}(\vec{x}, t))^T)$ has been replaced by the deformation gradient $\vec{\nabla} \vec{u}(\vec{x}, t)$ exploiting the total symmetry of the elastic stiffness tensor ${}^4\mathbf{C}_s = {}^4\mathbf{C}_s^{\text{RT}} = {}^4\mathbf{C}_s^{\text{LT}}$. Continuity of normal stress and normal displacements are imposed at the fluid-solid interface

$$\begin{aligned} \vec{u}(\vec{x}, t) \cdot \vec{n}_{fs}(\vec{x}) &= \vec{U}(\vec{x}, t) \cdot \vec{n}_{fs}(\vec{x}) \quad \text{for } (\vec{x}, t) \in \Gamma_{fs}^{\text{FULL}} \times [t_1, t_2], \\ \vec{\sigma}(\vec{x}, t) \cdot \vec{n}_{fs}(\vec{x}) &= -p(\vec{x}, t) \vec{n}_{fs}(\vec{x}) \quad \text{for } (\vec{x}, t) \in \Gamma_{fs}^{\text{FULL}} \times [t_1, t_2], \end{aligned} \quad (5)$$

where the normal to the interface \vec{n}_{fs} is considered time-independent owing to the small-strain approximation elaborated in the Appendix A. For completeness, the system of partial differential equations is subjected to boundary conditions, for instance, of Dirichlet type

$$\begin{aligned} \vec{u}(\vec{x}, t) &= \vec{u}_D(\vec{x}, t) \quad \text{for } (\vec{x}, t) \in \partial\Omega_s^{\text{FULL}} \times [t_1, t_2], \\ p(\vec{x}, t) &= p_D(\vec{x}, t) \quad \text{for } (\vec{x}, t) \in \partial\Omega_f^{\text{FULL}} \times [t_1, t_2], \end{aligned}$$

and initial conditions

$$\begin{aligned} \vec{u}(\vec{x}, t = t_1) &= \vec{u}_{t_1}(\vec{x}) \quad \text{and} \quad \dot{\vec{u}}(\vec{x}, t = t_1) = \dot{\vec{u}}_{t_1}(\vec{x}) \quad \text{for } \vec{x} \in \Omega_s^{\text{FULL}}, \\ p(\vec{x}, t = t_1) &= p_{t_1}(\vec{x}) \quad \text{and} \quad \dot{p}(\vec{x}, t = t_1) = \dot{p}_{t_1}(\vec{x}) \quad \text{for } \vec{x} \in \Omega_f^{\text{FULL}}. \end{aligned}$$

For simplicity, in the following, the explicit dependence of the fields on (\vec{x}, t) will be omitted.

2.2 | Macroscopic homogenized continuum

The fundamental concept of the variationally consistent homogenization is to assume that the macroscopic fields are conserved at the macroscopic level, Figure 1B, in the same fashion as given by the full field Equation (3). This assumption is referred to as the duality principle by Blanco⁴⁵ where the governing equations are generalized as moment rate-like and stress-like terms. Thus, the governing equations at the macroscopic level may be described by

$$\begin{aligned} \dot{\vec{\pi}}_M - \vec{\nabla}_M \cdot \vec{\sigma}_M^T &= \vec{0} \quad \text{in } \Omega_M \times [t_1, t_2], \\ -\dot{\vec{\epsilon}}_M + \vec{\nabla}_M \cdot \vec{\dot{U}}_M &= 0 \quad \text{in } \Omega_M \times [t_1, t_2]. \end{aligned} \quad (6)$$

Note, that both equations hold at every macroscopic position $\vec{x}_M \in \Omega_M$, where, in essence, both fluid and solid fields co-exist at the same position, see Figure 1B. On the contrary, in the full field problem, Figure 1A, a position vector \vec{x} lies in either fluid or solid domain. The so-far-undefined macroscopic constitutive relations will be discussed in Section 2.4; they will emerge from the scale coupling condition yielding a macroscopic problem that can be solved in terms of the macroscopic fields in a (\vec{u}_M, p_M) -formulation coupled to the micro-governing equations. The constitutive relations will be calculated from microstructural RVE simulations, for example, using the finite element method as will be demonstrated in Section 3. Subsequently, the macroscopic equations of the classical Biot theory will be recovered as a special limit case.

2.3 | The separation of scales

2.3.1 | Longwave regime

Classic homogenization theories typically define two characteristic (length) scales. When the macroscopic effective wavelength λ_M is significantly larger than the representative sizes of all relevant microscopic features within the representative volume element, microscopic inertial effects are negligible. The separation of scales holds when

$$l \ll \lambda_M, \quad \text{for all features in the RVE.} \quad (7)$$

In this regime, a direct averaging of the fluid and solid governing equations can be carried out, for instance, Pride et al.,⁸ leading to the classic Biot² equations of motion.

2.3.2 | Locally resonant regime

When a heterogeneous porous structure is composed of multiple materials with high contrast in properties, and/or various geometrical features (for example, cantilever beam or resonant cavities) considerably different representative wavelengths co-exist within the representative volume element at a given excitation frequency. For the sake of simplicity, let's assume that in the considered RVE, the structure can be categorized into a *host* domain and a *resonant* domain having the characteristic sizes $l^{(\text{host})}$ and $l^{(\text{resonator})}$, respectively. In the special case that the *resonant* domain is confined in a region surrounded by the *host* domain, for example, in a pattern of sparsely embedded resonators in a host domain, a local resonance phenomenon takes place—commonly exhibiting exotic macroscopic dynamic behavior for example, negative effective mass.

The local resonant regime is characterized by

$$l^{(\text{host})} \ll \lambda^{(\text{host})}, \quad \text{for all features in the host domain} \quad (8)$$

and

$$l^{(\text{resonator})} \sim \lambda^{(\text{resonator})}, \quad \text{for all features in the resonant domain.} \quad (9)$$

The above conditions were introduced in the context of computational homogenization of metamaterials^{34,39–44,46} and is called the relaxed separation of scales. In the context of composite solids, this condition occurs when there is

sufficient contrast between *host* and *resonant* domains, for example, stiffness and sound speed, as discussed in Auriault and Boutin.³⁸

2.4 | The scale coupling relations

First-order spatial computational homogenization⁹ expands the microscopic field variables in terms of the macroscopic fields and their gradients, revealing a clear resemblance with a Taylor expansion

$$\begin{aligned}\bar{\mathbf{u}} &= \bar{\mathbf{u}}_M + (\bar{\mathbf{x}} - \bar{\mathbf{x}}_R) \cdot (\bar{\nabla}_M \bar{\mathbf{u}}_M) + \bar{\omega}_u \quad \text{for } \bar{\mathbf{x}} \in \Omega_s, \\ \mathbf{p} &= \mathbf{p}_M + (\bar{\mathbf{x}} - \bar{\mathbf{x}}_R) \cdot (\bar{\nabla}_M \mathbf{p}_M) + \omega_p \quad \text{for } \bar{\mathbf{x}} \in \Omega_f.\end{aligned}\quad (10)$$

The micro-fluctuation fields $\bar{\omega}_u(\bar{\mathbf{x}}, t)$ and $\omega_p(\bar{\mathbf{x}}, t)$ are added to accommodate higher-order terms and the local variations that may develop within the RVE due to the presence of heterogeneities. Note that $\bar{\mathbf{u}}$ is only defined in the solid domain Ω_s ; and \mathbf{p} only in Ω_f . The position $\bar{\mathbf{x}}_R$ denotes a reference microscopic point that can be chosen arbitrarily in the classic first-order computational homogenization when inertial and body forces are absent.⁴⁷ For the special case of locally resonant metamaterials where microinertia matters, the position vector $\bar{\mathbf{x}}_R$ will be selected ensuring that macro- and micro-fields are connected in a physically meaningful way, see Section 3.

In the literature, the Hill-Mandel macrohomogeneity principle has been extensively used in the quasistatic regime to couple two scales by setting the volume average of the microscopic virtual power within the RVE equal to the macroscopic Virtual Power, for example, Kouznetsova et al.,⁴⁸ enforcing a variationally consistent energy relation between the two scales. Extensions to this scale coupling, including the inertial forces have also been proposed which was formalized in a unified theory by Blanco et al.⁴⁵ The weak formulation of the macroscopic problem (6) may be written for all admissible test functions $\delta \ddot{\mathbf{u}}_M$ and $\delta \mathbf{p}_M$ where the symbol $\delta(\cdot)$ denotes the variation as defined in Bedford.⁵ In variational calculus, the integral functional is derived from the Euler-Lagrange equations which, in this case, are the strong form (6) of the poroelastic problem. Since a macroscopic position $\bar{\mathbf{x}}_M$ is associated with a point with porosity ϕ , the total integral functional is written as

$$\int_{\Omega_M} (1 - \phi) \left\{ \dot{\bar{\mathbf{x}}}_M - \bar{\nabla}_M \cdot \boldsymbol{\sigma}_M^T \right\} \cdot \delta \ddot{\mathbf{u}}_M dV_M + \int_{\Omega_M} \phi \left\{ -\ddot{\epsilon}_M + \bar{\nabla}_M \cdot \ddot{\mathbf{U}}_M \right\} \delta \mathbf{p}_M dV_M = 0, \quad \forall (\delta \ddot{\mathbf{u}}_M, \delta \mathbf{p}_M). \quad (11)$$

Note that both terms in (11) have the same unit of power rate [W s⁻¹]. Using the divergence theorem, (11) can be rewritten as

$$\begin{aligned}& \int_{\Omega_M} (1 - \phi) \left\{ \dot{\bar{\mathbf{x}}}_M \cdot \delta \ddot{\mathbf{u}}_M + \boldsymbol{\sigma}_M : \delta \bar{\nabla}_M \ddot{\mathbf{u}}_M \right\} dV_M + \int_{\Omega_M} \phi \left\{ -\ddot{\epsilon}_M \delta \mathbf{p}_M - \ddot{\mathbf{U}}_M \cdot \delta \bar{\nabla}_M \mathbf{p}_M \right\} dV_M \\ &= \int_{\partial \Omega_M} (1 - \phi) (\boldsymbol{\sigma}_M \cdot \bar{\mathbf{n}}_M) \cdot \delta \ddot{\mathbf{u}}_M dA_M + \int_{\partial \Omega_M} -\phi (\ddot{\mathbf{U}}_M \cdot \bar{\mathbf{n}}_M) \delta \mathbf{p}_M dA_M, \quad \forall (\delta \ddot{\mathbf{u}}_M, \delta \mathbf{p}_M),\end{aligned}\quad (12)$$

where $\bar{\mathbf{n}}_M$ is the outward normal to the external boundary of the macroscopic domain Ω_M . In the left-hand side of the solid part of the Equation (12), the first term represents the kinetic power rate, and the second term represents the elastic power rate. In the left-hand side of the fluid part of the equation, the first term is related to the elastic power rate, and the second term gives the kinetic power rate. The right-hand side of the Equation (12) describes the external virtual power rate applied to the macroscopic surface. In summary, the integral functional (12), may be written in a compact form separating internal and external contributions as

$$\int_{\Omega_M} \delta I_M^{\text{int}} dV_M = \int_{\partial \Omega_M} \delta I_M^{\text{ext}} dA_M, \quad \forall (\delta \ddot{\mathbf{u}}_M, \delta \mathbf{p}_M). \quad (13)$$

A similar algebraic procedure is performed for the microscopic governing Equation (3) defined on a representative volume element $\Omega_s \cup \Omega_f$ yielding the integral functional of the microscopic fluid-structure interaction problem. Note, that there is a fundamental difference between the two problems; in the macroscopic domain, both primary fields co-exist at each material point throughout the volume Ω_M , while in the microscopic domain, the primary fields exist in distinct volumes

of each phase. The integral functional of the microscopic problem assumes the same form as the macroscopic problem (13) with the additional Γ_{fs} -internal interface terms, in the left-hand side, that correspond to the internal virtual power rate at the fluid-solid interface, leading to

$$\begin{aligned} & \int_{\Omega_s} \left\{ \dot{\vec{\pi}} \cdot \delta \ddot{\vec{u}} + \boldsymbol{\sigma} : \delta \nabla \ddot{\vec{u}} \right\} dV + \int_{\Omega_f} \left\{ -\dot{\vec{\epsilon}} \delta p - \ddot{\vec{U}} \cdot \delta \nabla p \right\} dV + \int_{\Gamma_{fs}} \left\{ (p \vec{n}_s) \cdot \delta \ddot{\vec{u}} + (\ddot{\vec{u}} \cdot \vec{n}_f) \delta p \right\} dA \\ &= \int_{\partial \Omega_s} (\boldsymbol{\sigma} \cdot \vec{n}_s) \cdot \delta \ddot{\vec{u}} dA + \int_{\partial \Omega_f} -(\ddot{\vec{U}} \cdot \vec{n}_f) \delta p dA, \quad \forall (\delta \ddot{\vec{u}}, \delta p), \end{aligned} \quad (14)$$

where \vec{n}_s and \vec{n}_f are the outward normal to the solid domain Ω_s and the fluid domain Ω_f , respectively. Relation (14) can, in short, be written as

$$\int_{\Omega_s \cup \Omega_f} \delta I^{\text{int}} dV + \int_{\Gamma_{fs}} \delta I_{fs}^{\text{int}} dA = \int_{\partial \Omega_s \cup \partial \Omega_f} \delta I^{\text{ext}} dA, \quad \forall (\delta \ddot{\vec{u}}, \delta p). \quad (15)$$

Finally, the link between a macroscopic poroelastic problem (13) and the microscopic fluid-structure interaction problem (15) is formulated by volume averaging the internal integral functionals throughout the RVE of volume V as follows

$$\delta I_M^{\text{int}} = \frac{1}{V} \left(\int_{\Omega_s \cup \Omega_f} \delta I^{\text{int}} dV + \int_{\Gamma_{fs}} \delta I_{fs}^{\text{int}} dA \right), \quad \forall (\delta \ddot{\vec{u}}_M, \delta \ddot{\vec{u}}, \delta p_M, \delta p). \quad (16)$$

for all admissible macro and micro fields.

Hence, (16) becomes

$$\begin{aligned} & (1 - \phi) \dot{\vec{\pi}}_M \cdot \delta \ddot{\vec{u}}_M + (1 - \phi) \boldsymbol{\sigma}_M : \delta \nabla_M \ddot{\vec{u}}_M - \phi \dot{\vec{\epsilon}}_M \delta p_M - \phi \ddot{\vec{U}}_M \cdot \nabla \delta p_M \\ &= \frac{1}{V} \left(\int_{\Omega_s} \left\{ \dot{\vec{\pi}} \cdot \delta \ddot{\vec{u}} + \boldsymbol{\sigma} : \delta \nabla \ddot{\vec{u}} \right\} dV + \int_{\Gamma_{fs}} (p \vec{n}_s) \cdot \delta \ddot{\vec{u}} dA \right) \\ &+ \frac{1}{V} \left(\int_{\Omega_f} \left\{ -\dot{\vec{\epsilon}} \delta p - \ddot{\vec{U}} \cdot \nabla \delta p \right\} dV + \int_{\Gamma_{fs}} (\ddot{\vec{u}} \cdot \vec{n}_f) \delta p dA \right), \quad \forall (\delta \ddot{\vec{u}}_M, \delta \ddot{\vec{u}}, \delta p_M, \delta p). \end{aligned} \quad (17)$$

Using Equation (14) on the right-hand side leads to

$$\begin{aligned} & (1 - \phi) \dot{\vec{\pi}}_M \cdot \delta \ddot{\vec{u}}_M + (1 - \phi) \boldsymbol{\sigma}_M : \delta \vec{\nabla}_M \ddot{\vec{u}}_M - \phi \dot{\vec{\epsilon}}_M \delta p_M - \phi \ddot{\vec{U}}_M \cdot \delta \vec{\nabla}_M p_M \\ &= \frac{1}{V} \int_{\partial \Omega_s} (\boldsymbol{\sigma} \cdot \vec{n}_s) \cdot \delta \ddot{\vec{u}} dA + \frac{1}{V} \int_{\partial \Omega_f} -(\ddot{\vec{U}} \cdot \vec{n}_f) \delta p dA, \quad \forall (\delta \ddot{\vec{u}}_M, \delta \ddot{\vec{u}}, \delta p_M, \delta p). \end{aligned} \quad (18)$$

Substituting the macro-to-micro relations (10) into (18) gives

$$\begin{aligned} & (1 - \phi) \dot{\vec{\pi}}_M \cdot \delta \ddot{\vec{u}}_M + (1 - \phi) \boldsymbol{\sigma}_M : \delta \vec{\nabla}_M \ddot{\vec{u}}_M - \phi \dot{\vec{\epsilon}}_M \delta p_M - \phi \ddot{\vec{U}}_M \cdot \delta \vec{\nabla}_M p_M \\ &= \frac{1}{V} \int_{\partial \Omega_s} (\boldsymbol{\sigma} \cdot \vec{n}_s) \cdot \left(\delta \ddot{\vec{u}}_M + (\vec{x} - \vec{x}_R) \cdot \delta \left(\vec{\nabla}_M \ddot{\vec{u}}_M \right) + \delta \ddot{\vec{\omega}}_u \right) dA \\ &+ \frac{1}{V} \int_{\partial \Omega_f} -(\ddot{\vec{U}} \cdot \vec{n}_f) \left(\delta p_M + (\vec{x} - \vec{x}_R) \cdot \delta \left(\vec{\nabla}_M p_M \right) + \delta \omega_p \right) dA, \quad \forall (\delta \ddot{\vec{u}}_M, \delta \ddot{\vec{\omega}}_u, \delta p_M, \delta \omega_p). \end{aligned} \quad (19)$$

Next, as typically done in computational homogenization methods, the virtual power rate of the micro-fluctuations on the boundary is requested to vanish

$$\begin{aligned} & \int_{\partial \Omega_s} (\boldsymbol{\sigma} \cdot \vec{n}_s) \cdot \delta \ddot{\vec{\omega}}_u dA = 0, \\ & \int_{\partial \Omega_f} -(\ddot{\vec{U}} \cdot \vec{n}_f) \delta \omega_p dA = 0. \end{aligned} \quad (20)$$

This can be ensured by, for instance, *zero uniform* or *periodic* boundary conditions on the micro-fluctuation fields. Specifically, in this contribution, the choice has been made to impose *periodic* conditions on the micro-fluctuation for the solid phase at the boundary and *zero uniform* conditions on the micro-fluctuation for the fluid boundary. Let $\Gamma_b = \{\vec{x}_1, \vec{x}_2, \vec{x}_3, \vec{x}_4\}$ be the set of corner position vectors of a rectangular (2D) representative volume element with $\Gamma_b \subset \partial\Omega_s$. Moreover, let the solid external boundary $\partial\Omega_s$ be split into “+” and “−” parts defining opposite boundaries with the outward normal vector at the corresponding points \vec{x}^+ and \vec{x}^- satisfying $\vec{n}_s(\vec{x}^+) = -\vec{n}_s(\vec{x}^-)$. The *periodic* boundary condition for the solid micro-fluctuation is

$$\begin{aligned}\vec{\omega}_u(\vec{x}^+) &= \vec{\omega}_u(\vec{x}^-), & \forall \vec{x} \in \partial\Omega_s, \\ \vec{\omega}_u(\vec{x}) &= \vec{0}, & \forall \vec{x} \in \Gamma_b,\end{aligned}\quad (21)$$

and has the advantage of predicting more accurately the homogenized material property for the longwave regime, compared to the *zero uniform* boundary condition, as shown by for example, Terada et al.⁴⁹ for the classic computational homogenization case. For the fluid phase, the *zero uniform* boundary condition on the micro-fluctuation is defined as

$$\omega_p(\vec{x}) = 0, \quad \forall \vec{x} \in \partial\Omega_f. \quad (22)$$

Periodic boundary conditions for the fluid would provide a more accurate prediction of the homogenized material properties of the fluid in the longwave regime. However, with such boundary conditions, the eigenmodes used as the local resonance basis discussed in Section 3.2, would introduce pressure variations at the RVE boundary, violating the scale separation hypothesis established in Section 2.3. The mode shape of the solid using *periodic* boundary conditions is practically the same as the mode shape using *zero uniform* boundary conditions, therefore, the periodicity is preferred for a better performance in the longwave regime. Note that to avoid the possible contradiction between the solid-fluid interface conditions (5) and the unit cell boundary conditions, the unit cell should be chosen such that the normal to the solid-fluid interface does not coincide with the normal to the unit cell boundary, that is, the interface should not lie along the unit cell boundary, which in most cases can be easily satisfied.

Finally, the virtual power rate integrals (20) vanish at the solid boundary thanks to the relation (21) and the antiperiodicity of solid traction,⁴⁹ whereas for the fluid it vanishes trivially thanks to relation (22). Since, Equation (19) must hold for all admissible macro- and micro-fields, the macroscopic constitutive relations are obtained as

$$\begin{aligned}(1 - \phi)\dot{\vec{\pi}}_M &= \frac{1}{V} \int_{\partial\Omega_s} (\boldsymbol{\sigma} \cdot \vec{n}_s) \, dA, & \phi\ddot{\epsilon}_M &= \frac{1}{V} \int_{\partial\Omega_f} (\ddot{\vec{U}} \cdot \vec{n}_f) \, dA, \\ (1 - \phi)\boldsymbol{\sigma}_M &= \frac{1}{V} \int_{\partial\Omega_s} (\boldsymbol{\sigma} \cdot \vec{n}_s) \otimes (\vec{x} - \vec{x}_R) \, dA, & \phi\ddot{\vec{U}}_M &= \frac{1}{V} \int_{\partial\Omega_f} (\ddot{\vec{U}} \cdot \vec{n}_f)(\vec{x} - \vec{x}_R) \, dA,\end{aligned}\quad (23)$$

which can be computed from the microstructural initial boundary value problem. Alternatively, relations (23) can be written in a more insightful form by applying the divergence theorem to the right-hand side of Equation (23), using the microscopic balance Equation (3) and the continuity at the solid-fluid interface (5) as

$$\begin{aligned}(1 - \phi)\dot{\vec{\pi}}_M &= \frac{1}{V} \int_{\Omega_s} \dot{\vec{\pi}} \, dV + \frac{1}{V} \int_{\Gamma_{fs}} p\vec{n}_s \, dA, \\ (1 - \phi)\boldsymbol{\sigma}_M &= \frac{1}{V} \int_{\Omega_s} \left\{ \boldsymbol{\sigma} + \dot{\vec{\pi}} \otimes (\vec{x} - \vec{x}_R) \right\} dV + \frac{1}{V} \int_{\Gamma_{fs}} p\vec{n}_s \otimes (\vec{x} - \vec{x}_R) \, dA, \\ \phi\ddot{\epsilon}_M &= \frac{1}{V} \int_{\Omega_f} \ddot{\epsilon} \, dV - \frac{1}{V} \int_{\Gamma_{fs}} \ddot{\vec{u}} \cdot \vec{n}_f \, dA, \\ \phi\ddot{\vec{U}}_M &= \frac{1}{V} \int_{\Omega_f} \left\{ \ddot{\vec{U}} + \ddot{\epsilon} (\vec{x} - \vec{x}_R) \right\} dV - \frac{1}{V} \int_{\Gamma_{fs}} \ddot{\vec{u}} \cdot \vec{n}_f (\vec{x} - \vec{x}_R) \, dA.\end{aligned}\quad (24)$$

The macroscopic constitutive relations (24), as such, do not assume time harmonic response as done in Gao et al.²² These relations should rather be interpreted as an extension of the solid-only equations proposed in Sridhar et al.⁴¹ for transient fluid-structure interaction problems. It is instructive to observe from Equation (24) that the conserved fields $\dot{\vec{\pi}}_M$ and $\ddot{\epsilon}_M$ are the volume averages of the corresponding microscopic fields with an additional interface term that includes

the contribution from the other phase, whereas, for the fluxes σ_M and \ddot{U}_M the volume integral involves not only the corresponding microscale quantities but also a non-trivial term related to a moment-like quantity of the microinertia with respect to the reference point \bar{x}_R . The inclusion of the microinertia contribution into the macroscopic flux was introduced by Molinari et al.⁵⁰ in the context of porous ductile materials under dynamic loading.

Finally, the relations linking the gradients of the field variables at both scales can be found by applying the gradient operator $\vec{\nabla}$ on the expressions (10), integrating over their respective phases, where the fields are defined, and using the divergence theorem, leading to

$$\begin{aligned}\vec{\nabla}_M \vec{u}_M &= \frac{1}{V_s} \int_{\Omega_s} \vec{\nabla} \vec{u} \, dV - \frac{1}{V_s} \int_{\Gamma_{fs}} \vec{n}_s \otimes \vec{\omega}_u \, dA - \frac{1}{V_s} \int_{\partial\Omega_s} \vec{n}_s \otimes \vec{\omega}_u \, dA, \\ \vec{\nabla}_M p_M &= \frac{1}{V_f} \int_{\Omega_f} \vec{\nabla} p \, dV - \frac{1}{V_f} \int_{\Gamma_{fs}} \vec{n}_f \omega_p \, dA - \frac{1}{V_f} \int_{\partial\Omega_f} \vec{n}_f \omega_p \, dA.\end{aligned}\quad (25)$$

Since *uniform* or *periodic* boundary conditions for the micro-fluctuation fields have been selected as given by (21) and (22), the integrals over the external RVE boundary vanish:

$$\begin{aligned}\int_{\partial\Omega_s} \vec{n}_s \otimes \vec{\omega}_u \, dA &= \mathbf{0}, \\ \int_{\partial\Omega_f} \vec{n}_f \omega_p \, dA &= \vec{0}.\end{aligned}\quad (26)$$

Therefore, taking into account that $V_s = (1 - \phi)V$ and $V_f = \phi V$, the gradient relations (25) become

$$\begin{aligned}(1 - \phi) \vec{\nabla}_M \vec{u}_M &= \frac{1}{V} \int_{\Omega_s} \vec{\nabla} \vec{u} \, dV - \frac{1}{V} \int_{\Gamma_{fs}} \vec{n}_s \otimes \vec{\omega}_u \, dA, \\ \phi \vec{\nabla}_M p_M &= \frac{1}{V} \int_{\Omega_f} \vec{\nabla} p \, dV - \frac{1}{V} \int_{\Gamma_{fs}} \vec{n}_f \omega_p \, dA.\end{aligned}\quad (27)$$

It is interesting to note that the gradient relation coupling scales (27) in the computational homogenization approach assumes a form similar to Slattery's averaging theorem^{7,8} that is used to derive the Biot equations and Darcy's law by direct averaging the strong governing equations when microinertia is neglected.

3 | FINITE ELEMENT IMPLEMENTATION

3.1 | The microscale fluid-structure interaction problem

Let's assume that an appropriate representative volume element for a poroelastic material has been selected, see Figure 1C. The weak forms (14) are used to solve the microscale fluid-structure interaction problem via the finite element method, given *periodic* boundary conditions (21) for the solid phase and *zero uniform* boundary conditions (22) for the fluid phase. The pressure and displacement fields are approximated using a finite element ansatz in terms of the nodal values $\vec{u}(t)$ and $p(t)$, and shape functions $\underline{N} = \underline{N}(\vec{x})$ written in the matrix form as $\vec{u}(\vec{x}, t) \approx \underline{N}^T(\vec{x}) \vec{u}(t)$ and $p(\vec{x}, t) \approx \underline{N}^T(\vec{x}) p(t)$. The test functions $\delta \vec{u}(\vec{x})$ and $\delta p(\vec{x})$ are approximated using the same shape functions, for which the Galerkin method is used, see Zienkiewicz et al.⁵¹ Inserting the discretized fields into the weak form (14) and considering that it must hold for all admissible test functions leads to the system of second-order ordinary differential equations written in a matrix format as

$$\begin{bmatrix} \underline{\mathbf{M}} & \underline{\vec{0}} \\ -\underline{\vec{C}}^T & Q \end{bmatrix} \begin{bmatrix} \ddot{\vec{u}} \\ \ddot{p} \end{bmatrix} + \begin{bmatrix} \underline{\mathbf{K}} & \underline{\vec{C}} \\ \underline{\vec{0}} & H \end{bmatrix} \begin{bmatrix} \vec{u} \\ p \end{bmatrix} = \begin{bmatrix} \underline{\vec{f}}^{\text{ext}} \\ -q^{\text{ext}} \end{bmatrix}.\quad (28)$$

In (28), it is assumed that the dependent nodes due to the *periodic* boundary conditions of the solid boundary have already been eliminated similarly as, for instance, in References 41 and 48.

TABLE 1 The RVE nodes are sorted: b, b' are the prescribed nodes at the boundary and i, i' are the “independent” nodes.

	Set of prescribed nodes (at the boundary)	Set of independent nodes
solid phase	b (RVE corners only)	i
fluid phase	b'	i'
aggregate	$B = b \cup b'$	$I = i \cup i'$

Note: The matrices are rearranged accordingly, see Equation (B1) in the Appendix.

In the solid phase, $\underline{\mathbf{M}}$ is the mass matrix, and $\underline{\mathbf{K}}$ is the stiffness matrix. For the fluid phase, $\underline{\mathbf{Q}}$ is the matrix related to the volumetric strain energy and $\underline{\mathbf{H}}$, to the kinetic energy, while matrix $\underline{\mathbf{C}}$ appears from the coupling surface terms at Γ_{fs} . On the right-hand side, $\tilde{\mathbf{f}}^{\text{ext}}$ is the external force vector applied to the solid phase boundary, whereas $\tilde{\mathbf{q}}^{\text{ext}}$ is the external acceleration flux imposed at the fluid phase boundary.

The system (28) is non-symmetric due to the choice of $\tilde{\mathbf{u}}$ and \mathbf{p} as primary unknown fields causing the interface coupling terms $\underline{\mathbf{C}}$ and $\underline{\mathbf{C}}^T$ to appear in different matrices. A symmetric system is achieved, for instance, when $\tilde{\mathbf{u}}$ and $\tilde{\mathbf{U}}$ are chosen as primary unknown fields. The non-symmetry of the matrices is not optimal from the standard finite element solver viewpoint. Nonetheless, thanks to the choice of the pressure disturbance as a primary variable, the fluid automatically supports only irrotational displacements which are described in terms of volumetric strains. As Marburg and Nolte⁵² point out, this choice avoids the appearance of spurious modes in the fluid-structure eigenvalue problem. When a time-harmonic response is considered, the system (28) has real positive eigenvalues despite the lack of symmetry. It has been demonstrated in Sandberg⁵³ that through a sequence of eigenvalue-preserving transformations, the $(\tilde{\mathbf{u}}, \mathbf{p})$ system can be symmetrized, thereby, having real positive eigenvalues, as is expected, since the dynamic response of a conservative system does not decay with time. An additional advantage is that the discretized problem using the $(\tilde{\mathbf{u}}, \mathbf{p})$ -formulation has fewer degrees of freedom than the displacement $(\tilde{\mathbf{u}}, \tilde{\mathbf{U}})$ -formulation.

The matrix Equation (28) written in terms of the state vector $\underline{\mathbf{w}} = [\tilde{\mathbf{u}} \ \mathbf{p}]^T$ provides a compact form that greatly simplifies the matrix projections to be performed in Section 3.2, whereas in Section 3.3, the state vector will be again written as $[\tilde{\mathbf{u}} \ \mathbf{p}]^T$ for computing the fluid and solid responses separately. Hence, Equation (28) takes the compact form

$$\underline{\lambda} \underline{\ddot{\mathbf{w}}} + \underline{\mu} \underline{\mathbf{w}} = \underline{\mathbf{f}}^{\text{ext}}, \quad (29)$$

where $\underline{\lambda}$, $\underline{\mu}$, and $\underline{\mathbf{f}}^{\text{ext}}$ are the generalized mass matrix, stiffness matrix, and external load, respectively. Furthermore, the nodes may be split into the nodes at the boundary where the essential boundary conditions are prescribed, denoted by “B,” and the remaining “independent” nodes denoted by “I”. Finally, Equation (29) is partitioned according to Table 1 into

$$\begin{bmatrix} \underline{\lambda}_{BB} & \underline{\lambda}_{BI} \\ \underline{\lambda}_{IB} & \underline{\lambda}_{II} \end{bmatrix} \begin{bmatrix} \underline{\ddot{\mathbf{w}}}_B \\ \underline{\ddot{\mathbf{w}}}_I \end{bmatrix} + \begin{bmatrix} \underline{\mu}_{BB} & \underline{\mu}_{BI} \\ \underline{\mu}_{IB} & \underline{\mu}_{II} \end{bmatrix} \begin{bmatrix} \underline{\mathbf{w}}_B \\ \underline{\mathbf{w}}_I \end{bmatrix} = \begin{bmatrix} \underline{\mathbf{f}}_B^{\text{ext}} \\ \underline{\mathbf{Q}}_I \end{bmatrix}. \quad (30)$$

See Appendix B for the detailed definition of the submatrices. The columns of the state variables and the external loads are shown below.

$$\underline{\mathbf{w}}_B = \begin{bmatrix} \tilde{\mathbf{u}}_b \\ \mathbf{p}_{b'} \end{bmatrix} \quad \underline{\ddot{\mathbf{w}}}_I = \begin{bmatrix} \ddot{\tilde{\mathbf{u}}}_i \\ \ddot{\mathbf{p}}_{i'} \end{bmatrix} \quad \underline{\mathbf{f}}_B^{\text{ext}} = \begin{bmatrix} \tilde{\mathbf{f}}_b^{\text{ext}} \\ -\mathbf{q}_{b'}^{\text{ext}} \end{bmatrix} \quad \underline{\mathbf{Q}}_I = \begin{bmatrix} \tilde{\mathbf{Q}}_i \\ \mathbf{Q}_{i'} \end{bmatrix} \quad (31)$$

Since the system of Equation (30) is simply the rearranged system (28), its sub-matrices are also non-symmetric.

3.2 | Macroscale problem: Projection on the reduced space

At this stage, the equivalent macroscale initial boundary value problem, Figure 1B, obtained through the computational homogenization approach, is governed by the macroscopic Equation (6) coupled to the discretized system of ordinary

differential Equation (30) with I-number of unknowns. The coupling between the scales is given through the microscale boundary condition, using the relation (10), where at the B prescribed nodes, the micro-fluctuations are given by (21) and (22). Hence, the macroscopic equivalent problem could be solved via, for example, the finite element method in a $(\bar{\mathbf{u}}_M, \mathbf{p}_M, \mathbb{W}_I)$ -formulation, where the I unknown nodal fields can be interpreted as internal variables that satisfy the evolution Equation (30), as done in FE² type methods, for example, by Pham et al.³⁹ and Van Nuland et al.⁴⁰ Instead, in the following, a reduced basis characteristic for a locally resonant dynamic material response will be used, significantly decreasing the number of internal variables I.

In general, model reduction techniques aim at finding a set of variables that can express the sought solution of a problem with a lower number of degrees of freedom through a base change. Typically, when the overall solution pattern is known a priori, a well-suited reduced basis can be found. In the context of the microscale governing equations that were discretized via the finite element method in Section 3.1, the objective is to express the internal variables \mathbb{W}_I in a reduced space. For the considered problem, two distinct and approximately superimposable solutions can be identified for the construction of a representative reduced basis. The first solution assumes the full separation of scales, that is, the longwave regime defined in Section 2.3.1. In this case, the microscale problem is well approximated by a steady-state condition given by

$$\begin{aligned}\vec{\nabla} \cdot \boldsymbol{\sigma}^T &= \vec{0}, & \text{in } \Omega_s \times t, \\ \vec{\nabla} \cdot \ddot{\mathbf{U}} &= 0, & \text{in } \Omega_f \times t.\end{aligned}\quad (32)$$

The solution of the steady-state problem (32) implies an instantaneous response of the RVE for a given macroscopic state $(\bar{\mathbf{u}}_M, \mathbf{p}_M, \vec{\nabla}_M \bar{\mathbf{u}}_M, \vec{\nabla}_M \mathbf{p}_M)$, defined by (10) with boundary conditions (21) and (22). The latter solution can be used to construct the so-called longwave basis that allows a variable change that eliminates completely the internal variables \mathbb{W}_I . Through the lens of the reduced basis approach, the classic computational homogenization can be viewed as the full dynamic response (30) projected onto the reduced longwave basis originating from the steady-state solution of (32).

The second solution stems from the time-harmonic microscale boundary value problem, obtained by using the $e^{+i\omega t}$ convention, where ω is the frequency in $[\text{rad s}^{-1}]$:

$$\begin{aligned}-\omega^2 \rho_s \bar{\mathbf{u}} - \vec{\nabla} \cdot (\mathbf{C}_s : \vec{\nabla} \bar{\mathbf{u}}) &= \vec{0} & \text{in } \Omega_s, \\ -\frac{\omega^2}{K_f} \mathbf{p} - \vec{\nabla} \cdot \left(\frac{1}{\rho_f} \vec{\nabla} \mathbf{p} \right) &= 0 & \text{in } \Omega_f,\end{aligned}\quad (33)$$

subjected to Dirichlet boundary conditions on the B prescribed nodes, that is, assuming that the host domain at the boundary is practically in a long wavelength regime relative to the internal nodes, that is, in accordance with the relaxed separation of scales condition established in Section 2.3.2. The solution of the time-harmonic boundary value problem (33) provides the identification of the so-called spectral basis. The spectral basis allows to reduce the internal variables \mathbb{W}_I to the Q lowest relevant eigenmode amplitudes η_Q , with typically $Q \ll I$. A small, and yet representative, spectral basis generated under zero Dirichlet boundary conditions works successfully, as long as the dynamic behavior of The RVE is localized inside the host medium, as demonstrated by Sridhar et al.⁴¹ for a solid-only metamaterial case and which is extended here to the fluid-structure problem. Therefore, based on the above considerations, for a fluid-structure RVE that satisfies the relaxed separation of scales, the solution can be represented as the superposition of the longwave and local resonance solutions:

$$\mathbb{W} \approx \mathbb{W}_{\text{longwave}} + \mathbb{W}_{\text{local resonance}} = \begin{bmatrix} \mathbb{W}_B \\ \mathbb{W}_I^{(lw)} \end{bmatrix} + \begin{bmatrix} \mathbb{Q}_B \\ \mathbb{W}_I^{(lr)} \end{bmatrix} = \begin{bmatrix} \mathbb{W}_B \\ \mathbb{W}_I^{(lw)} + \mathbb{W}_I^{(lr)} \end{bmatrix}. \quad (34)$$

Next, the longwave solution $\mathbb{W}_I^{(lw)}$ is expressed by projecting it onto the longwave basis, computed via a steady-state BVP (32), while the local resonance solution $\mathbb{W}_I^{(lr)}$ will be expressed through the reduced spectral basis, computed via the time-harmonic BVP (33), as elaborated in the following.

The discrete form of the longwave Equation (32) is obtained by disregarding the generalized inertial terms in Equation (30). From there, $\mathbb{W}_I^{(lw)}$ can be expressed in terms of the left $\underline{\mathbb{Y}}$ and right $\underline{\mathbb{S}}$ longwave bases as

$${}^L\mathbb{W}_I^{(lw)} = \mathbb{Y} \mathbb{W}_B \quad \text{and} \quad {}^R\mathbb{W}_I^{(lw)} = \mathbb{S} \mathbb{W}_B \quad (35)$$

$$\text{with } \mathbb{Y}^T = -\underline{\mu}_{BI} \underline{\mu}_{II}^{-1} \quad \text{and} \quad \mathbb{S} = -\underline{\mu}_{II}^{-1} \underline{\mu}_{IB}. \quad (36)$$

Note, that the distinction between the right and left bases is made here because of the non-symmetry of the system, as discussed before.

The discretized left and right time-harmonic problems (33) are given by

$$\left[-\omega_j^2 \underline{\lambda}_{II}^T + \underline{\mu}_{II}^T \right] \underline{\Psi}_I^{(j)} = \underline{\mathbb{Q}}_I \quad \text{and} \quad \left[-\omega_j^2 \underline{\lambda}_{II} + \underline{\mu}_{II} \right] \underline{\Phi}_I^{(j)} = \underline{\mathbb{Q}}_I \quad (37)$$

with $\underline{\Psi}_I^{(j)}$ and $\underline{\Phi}_I^{(j)}$ the j th left and right eigenmodes, respectively, where $j = 1, \dots, I$. Next, a selection of Q lowest localized resonant modes will be made, with the truncation $Q \ll I$. The selected left and right modes are collected in the matrices $\underline{\Psi}$ and $\underline{\Phi}$, respectively. Thus, the internal field variables in the local resonance solution are approximated using the truncated spectral bases

$${}^L\mathbb{W}_I^{(lr)} \approx \underline{\Psi} \underline{\eta}_Q \quad \text{and} \quad {}^R\mathbb{W}_I^{(lr)} \approx \underline{\Phi} \underline{\eta}_Q \quad (38)$$

with $\underline{\eta}_Q$ the column with the (scalar) mode amplitudes. The matrices $\underline{\Psi}$ and $\underline{\Phi}$, which here are referred to as “local resonance” bases, are normalized with respect to the generalized mass matrix, that is, satisfying

$$\underline{\Psi}^T \underline{\lambda}_{II} \underline{\Phi} = \underline{I}_{QQ}^{(lr)} \quad (39)$$

with $\underline{I}_{QQ}^{(lr)}$ the unit matrix of the appropriate dimension. As a direct consequence, the generalized stiffness matrix expressed in the modal basis is a diagonal matrix

$$\underline{\Lambda}_{QQ}^{(lr)} = \underline{\Psi}^T \underline{\mu}_{II} \underline{\Phi} \quad (40)$$

containing the truncated eigenvalues ω_j^2 , where $j = 1, \dots, Q$. Collecting (35) and (38) into (34), the left and right basis transformations are expressed as

$$\begin{bmatrix} {}^L\mathbb{W}_B \\ {}^L\mathbb{W}_I \end{bmatrix} = \begin{bmatrix} \underline{\mathbb{O}} & \underline{\mathbb{I}} \\ \underline{\Psi} & \underline{\mathbb{Y}} \end{bmatrix} \begin{bmatrix} \underline{\eta}_Q \\ \mathbb{W}_B \end{bmatrix} \quad \text{and} \quad \begin{bmatrix} {}^R\mathbb{W}_B \\ {}^R\mathbb{W}_I \end{bmatrix} = \begin{bmatrix} \underline{\mathbb{O}} & \underline{\mathbb{I}} \\ \underline{\Phi} & \underline{\mathbb{S}} \end{bmatrix} \begin{bmatrix} \underline{\eta}_Q \\ \mathbb{W}_B \end{bmatrix}, \quad (41)$$

where $\underline{\mathbb{O}}$ and $\underline{\mathbb{I}}$ are the zero and unit matrices of appropriate dimensions, respectively. Equation (30) can then be projected on the new, reduced basis

$$\begin{bmatrix} \underline{\mathbb{O}} & \underline{\mathbb{I}} \\ \underline{\Psi} & \underline{\mathbb{Y}} \end{bmatrix}^T \begin{bmatrix} \underline{\lambda}_{BB} & \underline{\lambda}_{BI} \\ \underline{\lambda}_{IB} & \underline{\lambda}_{II} \end{bmatrix} \begin{bmatrix} \underline{\mathbb{O}} & \underline{\mathbb{I}} \\ \underline{\Phi} & \underline{\mathbb{S}} \end{bmatrix} \begin{bmatrix} \underline{\eta}_Q \\ \underline{\dot{\mathbb{W}}}_B \end{bmatrix} + \begin{bmatrix} \underline{\mathbb{O}} & \underline{\mathbb{I}} \\ \underline{\Psi} & \underline{\mathbb{Y}} \end{bmatrix}^T \begin{bmatrix} \underline{\mu}_{BB} & \underline{\mu}_{BI} \\ \underline{\mu}_{IB} & \underline{\mu}_{II} \end{bmatrix} \begin{bmatrix} \underline{\mathbb{O}} & \underline{\mathbb{I}} \\ \underline{\Phi} & \underline{\mathbb{S}} \end{bmatrix} \begin{bmatrix} \underline{\eta}_Q \\ \mathbb{W}_B \end{bmatrix} = \begin{bmatrix} \underline{\mathbb{O}} & \underline{\mathbb{I}} \\ \underline{\Psi} & \underline{\mathbb{Y}} \end{bmatrix}^T \begin{bmatrix} \underline{\mathbb{f}}_B^{\text{ext}} \\ \underline{\mathbb{Q}}_I \end{bmatrix} \quad (42)$$

leading to

$$\underline{I}_{QQ}^{(lr)} \underline{\eta}_Q + \underline{\Lambda}_{QQ}^{(lr)} \underline{\eta}_Q = -\underline{\lambda}_{QB}^{(c)} \underline{\dot{\mathbb{W}}}_B \quad (43)$$

$$\underline{\lambda}_{BB}^{(lw)} \underline{\dot{\mathbb{W}}}_B + \underline{\mu}_{BB}^{(lw)} \mathbb{W}_B + \underline{\lambda}_{BQ}^{(c)} \underline{\eta}_Q = \underline{\mathbb{f}}_B^{\text{ext}}, \quad (44)$$

where $\underline{\lambda}_{BB}^{(lw)}$, $\underline{\mu}_{BB}^{(lw)}$, $\underline{\lambda}_{BQ}^{(c)}$, and $\underline{\lambda}_{QB}^{(c)}$ are the finite element submatrices of (30) projected onto the reduced basis as shown in Equation (42), see Appendix B for the detailed expressions. Note that the coupling between the local resonance dynamics (43) and the longwave dynamics (44), given by the matrices $\underline{\lambda}_{QB}^{(c)}$ and $\underline{\lambda}_{BQ}^{(c)}$, is purely driven by the inertial forces as these matrices depend only on the generalized mass matrix $\underline{\lambda}$ and the reduced basis (Appendix B).

The discretized system of Equation (30) describes the fully resolved dynamics of the RVE, whereas the projected system of Equations (43),(44) provides the RVE dynamics expressed in the reduced basis that, in general, does not represent the full dynamical response. Typically, the validity of the solution provided by the reduced system is limited by the frequency of the highest localized mode included in the reduced basis. This is not a severe restriction if the frequency spectrum of interest is known beforehand, which is the case for most applications. As a remark, it should be noted that the assumed decomposition (34) is in line with well-known model order reduction techniques, typically used in structural dynamics, based on the substructuring of a problem into superelements to compute the overall dynamic response of a large structure. For fluid-structure interaction problems, it has been applied with great success, for example, in References 54–58. In a multiscale context, the RVE can be considered a substructure of the macroscopic problem.

3.3 | Upscaling reduced microscale response

Next, the microscale response expressed in terms of the reduced longwave and local resonance bases, will be coupled to the macroscale response given by expressions (23), which in discrete form are written as

$$\begin{aligned} (1 - \phi) \dot{\vec{\pi}}_M &= \frac{1}{V} \mathbf{1}_b^T \vec{f}_b^{\text{ext}} & \phi \ddot{\epsilon}_M &= \frac{1}{V} \mathbf{1}_{b'}^T \vec{q}_{b'}^{\text{ext}}, \\ (1 - \phi) \sigma_M &= \frac{1}{V} \left(\vec{f}_b^{\text{ext}} \right)^T \otimes \Delta \vec{x}_b & \phi \ddot{\vec{U}}_M &= \frac{1}{V} \left(\vec{q}_{b'}^{\text{ext}} \right)^T \Delta \vec{x}_{b'}, \end{aligned} \quad (45)$$

where $\mathbf{1}_b$ and $\mathbf{1}_{b'}$ are columns with scalar unit components. The notation $\Delta \vec{x} = \vec{x} - \vec{x}_R$ is introduced for a position vector on the RVE boundary $\vec{x} \in \partial\Omega_s \cup \partial\Omega_f$. Thus, in the discrete form, it is written as $\Delta \vec{x}_b$ and $\Delta \vec{x}_{b'}$ for solid and fluid boundaries, respectively.

Substituting $\vec{f}_b^{\text{ext}} = [\vec{f}_b^{\text{ext}} - \vec{q}_{b'}^{\text{ext}}]^T$ defined in (31) into (44), and taking into account that $\mathbb{W}_B = [\vec{u}_b \quad \vec{p}_{b'}]^T$ with

$$\begin{aligned} \vec{u}_b &= \mathbf{1}_b \vec{u}_M + \Delta \vec{x}_b \cdot \vec{\nabla}_M \vec{u}_M, \\ \vec{p}_{b'} &= \mathbf{1}_{b'} \vec{p}_M + \Delta \vec{x}_{b'} \cdot \vec{\nabla}_M \vec{p}_M, \end{aligned} \quad (46)$$

which follow from (10). Taking into account the boundary conditions (21) and (22), results in a closed-form expression of the constitutive relations for the macroscopic solid momentum $\vec{\pi}_M$, macroscopic solid stress σ_M , macroscopic fluid volumetric strain ϵ_M , and macroscopic fluid displacement \vec{U}_M as functions of the macroscopic state $(\vec{u}_M, \vec{p}_M, \vec{\nabla}_M \vec{u}_M, \vec{\nabla}_M \vec{p}_M)$ and the resonant modes amplitudes η_Q

$$\begin{aligned} (1 - \phi) \dot{\vec{\pi}}_M &= \mathbf{A}_\pi \cdot \ddot{\vec{u}}_M + {}^3\mathbf{B}_\pi : \ddot{\vec{\nabla}} \vec{u}_M + \vec{C}_\pi \ddot{\vec{p}}_M + \mathbf{D}_\pi \cdot \ddot{\vec{\nabla}} \vec{p}_M \\ &\quad + \mathbf{E}_\pi \cdot \ddot{\vec{u}}_M + {}^3\mathbf{F}_\pi : \ddot{\vec{\nabla}} \vec{u}_M + \vec{G}_\pi \ddot{\vec{p}}_M + \mathbf{H}_\pi \cdot \ddot{\vec{\nabla}} \vec{p}_M + \sum_{j=1}^Q \vec{a}_j \ddot{\eta}_j, \\ (1 - \phi) \sigma_M &= {}^3\mathbf{A}_\sigma \cdot \ddot{\vec{u}}_M + {}^4\mathbf{B}_\sigma : \ddot{\vec{\nabla}} \vec{u}_M + \mathbf{C}_\sigma \ddot{\vec{p}}_M + {}^3\mathbf{D}_\sigma \cdot \ddot{\vec{\nabla}} \vec{p}_M \\ &\quad + {}^3\mathbf{E}_\sigma \cdot \ddot{\vec{u}}_M + {}^4\mathbf{F}_\sigma : \ddot{\vec{\nabla}} \vec{u}_M + \mathbf{G}_\sigma \ddot{\vec{p}}_M + {}^3\mathbf{H}_\sigma \cdot \ddot{\vec{\nabla}} \vec{p}_M + \sum_{j=1}^Q \mathbf{b}_j \ddot{\eta}_j, \\ \phi \ddot{\epsilon}_M &= \vec{A}_\epsilon \cdot \ddot{\vec{u}}_M + \mathbf{B}_\epsilon : \ddot{\vec{\nabla}} \vec{u}_M + \vec{C}_\epsilon \ddot{\vec{p}}_M + \vec{D}_\epsilon \cdot \ddot{\vec{\nabla}} \vec{p}_M \\ &\quad + \vec{E}_\epsilon \cdot \ddot{\vec{u}}_M + \mathbf{F}_\epsilon : \ddot{\vec{\nabla}} \vec{u}_M + \vec{G}_\epsilon \ddot{\vec{p}}_M + \vec{H}_\epsilon \cdot \ddot{\vec{\nabla}} \vec{p}_M + \sum_{j=1}^Q c_j \ddot{\eta}_j, \\ \phi \ddot{\vec{U}}_M &= \mathbf{A}_U \cdot \ddot{\vec{u}}_M + {}^3\mathbf{B}_U : \ddot{\vec{\nabla}} \vec{u}_M + \vec{C}_U \ddot{\vec{p}}_M + \mathbf{D}_U \cdot \ddot{\vec{\nabla}} \vec{p}_M \\ &\quad + \mathbf{E}_U \cdot \ddot{\vec{u}}_M + {}^3\mathbf{F}_U : \ddot{\vec{\nabla}} \vec{u}_M + \vec{G}_U \ddot{\vec{p}}_M + \mathbf{H}_U \cdot \ddot{\vec{\nabla}} \vec{p}_M + \sum_{j=1}^Q \vec{d}_j \ddot{\eta}_j, \end{aligned} \quad (47)$$

where the upper-case material property coefficients, from A_ξ to H_ξ , alphabetically, with index $\xi = \{\pi, \sigma, \epsilon, U\}$, correspond to the longwave regime, and the lower-case ones, \vec{a}_j , \vec{b}_j , \vec{c}_j , and \vec{d}_j are the material property coefficients of mode j , corresponding to the local resonance regime.

Combining Equation (43) with (46), yields the evolution equation for the internal dynamic variables η_Q

$$\ddot{\eta}_j + \omega_j^2 \eta_j = - \vec{a}_j \cdot \ddot{\vec{u}}_M - \vec{\beta}_j : \ddot{\vec{V}}_M \ddot{\vec{u}}_M + \gamma_j \ddot{p}_M + \vec{\delta}_j \cdot \ddot{\vec{V}}_M \ddot{p}_M, \quad \text{for eigenmodes } j = 1, 2, \dots, Q, \quad (48)$$

where ω_j is the eigenfrequency of mode j , and \vec{a}_j , $\vec{\beta}_j$, γ_j , and $\vec{\delta}_j$ are the homogenized material coefficients of mode j , corresponding to the local resonance regime. The detailed derivations leading to constitutive relations (47) and the evolution Equation (48), as well as the final expressions of the homogenized coefficients, are given in Appendix C.

Note that several coefficients in (47) are identically zero: \mathbf{E}_π , ${}^3\mathbf{F}_\pi$, ${}^3\mathbf{E}_\sigma$, \vec{E}_ϵ , \mathbf{F}_ϵ , G_ϵ , \vec{H}_ϵ , \mathbf{E}_U , ${}^3\mathbf{F}_U$, and \vec{G}_U ; or approximately zero \vec{C}_π , \mathbf{D}_π , \vec{G}_π , \mathbf{C}_σ , ${}^3\mathbf{D}_\sigma$, ${}^4\mathbf{B}_\sigma$, ${}^3\mathbf{H}_\sigma$, A_ϵ , \mathbf{B}_U , and \mathbf{D}_U . See Appendix C for details.

The governing equations of the equivalent macroscopic problem depicted in Figure 1B are, therefore, the collection of the two conservation Equation (6) together with the Q evolution Equation (48)

$$\begin{cases} \dot{\vec{\pi}}_M = \ddot{\vec{V}} \cdot \vec{\sigma}_M^T, \\ \ddot{\vec{\epsilon}}_M = \ddot{\vec{V}} \cdot \ddot{\vec{U}}_M, \\ \ddot{\eta}_j + \omega_j^2 \eta_j = - \vec{a}_j \cdot \ddot{\vec{u}}_M - \vec{\beta}_j : \ddot{\vec{V}}_M \ddot{\vec{u}}_M + \gamma_j \ddot{p}_M + \vec{\delta}_j \cdot \ddot{\vec{V}}_M \ddot{p}_M, \end{cases} \quad \text{for eigenmodes } j = 1, 2, \dots, Q, \quad (49)$$

and constitutive relations

$$\begin{aligned} (1 - \phi) \dot{\vec{\pi}}_M &= \mathbf{A}_\pi \cdot \ddot{\vec{u}}_M + {}^3\mathbf{B}_\pi : \ddot{\vec{V}} \ddot{\vec{u}}_M + \mathbf{H}_\pi \cdot \ddot{\vec{V}} p_M + \sum_{j=1}^Q \vec{a}_j \ddot{\eta}_j, \\ (1 - \phi) \sigma_M &= {}^3\mathbf{A}_\sigma \cdot \ddot{\vec{u}}_M + {}^4\mathbf{F}_\sigma : \ddot{\vec{V}} \ddot{\vec{u}}_M + \mathbf{G}_\sigma p_M + \sum_{j=1}^Q \vec{b}_j \ddot{\eta}_j, \\ \phi \ddot{\epsilon}_M &= \mathbf{B}_\epsilon : \ddot{\vec{V}} \ddot{\vec{u}}_M + C_\epsilon \ddot{p}_M + \vec{D}_\epsilon \cdot \ddot{\vec{V}} \ddot{p}_M + \sum_{j=1}^Q \vec{c}_j \ddot{\eta}_j, \\ \phi \ddot{\vec{U}}_M &= \mathbf{A}_U \cdot \ddot{\vec{u}}_M + \vec{C}_U \ddot{p}_M + \mathbf{H}_U \cdot \ddot{\vec{V}} p_M + \sum_{j=1}^Q \vec{d}_j \ddot{\eta}_j. \end{aligned} \quad (50)$$

The so-called (longwave) Biot coefficients

$$\mathbf{A}_\pi, \mathbf{H}_\pi, {}^4\mathbf{F}_\sigma, \mathbf{G}_\sigma, \mathbf{B}_\epsilon, C_\epsilon, \mathbf{A}_U, \mathbf{H}_U \quad (51)$$

refer to the terms that are predicted in the constitutive model proposed by Biot² and they are typically non-negligible, as expected of classic poroelastic materials. Coefficients (${}^3\mathbf{B}_\pi$, ${}^3\mathbf{A}_\sigma$, \vec{D}_ϵ , \vec{C}_U) have a nature similar to the so-called Willis coefficients.^{59,60} These may or may not vanish depending on the RVE symmetries and the specific choice of \vec{x}_R , for example, placed at the RVE centroid.

The local resonance coefficients

$$\vec{a}, \vec{b}, \vec{c}, \vec{d}, \vec{\alpha}, \vec{\beta}, \vec{\gamma}, \vec{\delta}, \quad (52)$$

depend, in general, on the nature of the occurring localized resonance. Typically, monopolar resonances, inducing a negative bulk modulus, lead to large coefficients (\vec{b} , $\vec{\beta}$) in solid, and (\vec{c} , $\vec{\gamma}$), in fluid. On the other hand, dipolar resonances inducing negative effective mass, result in large coefficients (\vec{a} , $\vec{\alpha}$), and, (\vec{d} , $\vec{\delta}$), in solid and fluid, respectively.

To summarize, at the macroscale, an enriched homogenized continuum has emerged. The internal dynamic variables \mathbb{w}_I , governed by Equation (30), were projected onto the reduced space identified in Section 3.2 and upscaled as a superposition of the longwave and local resonance responses in Section 3.3. As long as the internal dynamics is localized, the homogenized material behavior can be represented beyond the longwave regime through the incorporation of the additional internal variables η_Q into the constitutive relation (47), based on the relaxed separation of scales defined

in Section 2.3.2. In essence, through the evolution Equation (48) the motion of the *resonant* domain is coupled to the motion of the *host* domain. Therefore, a macroscopic (\vec{u}_M, p_M, η_Q) -formulation arises with additional internal variable fields that represent the underlying mode contribution to the overall macroscopic dynamics. The macroscopic problem can be discretized using for example, the finite element method and solved for given initial and boundary conditions.

3.4 | Effective Biot continuum

The considered longwave response of a solid-fluid aggregate corresponds to the “high-frequency limit case” where the leading order behavior can be assumed inviscid as considered in Biot.² In this regime, the boundary layers in the fluid become small compared to the pore size, and the microscopic fluid flow can be approximated by incompressible and inviscid behavior as described by the boundary value problem (32). This is called the breakdown of Poiseuille flow, indicating the entrance into the regime where the inertial forces are dominant. Note that, despite being named “high-frequency limit case,” the separation of scales still holds, that is, the propagating wavelength is much larger than the microscopic features.

In the longwave regime, that is, neglecting the local resonance-related terms, the obtained homogenized continuum reduces to a special case of the Biot model in the inviscid “high-frequency limit.” Indeed, considering only the coefficients (51) present in the Biot theory, the effective macroscopic governing equations of the homogenized poroelastic continuum in the longwave regime may be simplified to

$$\begin{aligned} \mathbf{A}_\pi \cdot \ddot{\vec{u}}_M + \mathbf{H}_\pi \cdot \vec{\nabla} p_M &= \vec{\nabla} \cdot \left({}^4\mathbf{F}_\sigma : \vec{\nabla} \vec{u}_M + \mathbf{G}_\sigma p_M \right), \\ \mathbf{B}_\epsilon : \vec{\nabla} \ddot{\vec{u}}_M + C_\epsilon \ddot{p}_M &= \vec{\nabla} \cdot \left(\mathbf{A}_U \cdot \ddot{\vec{u}}_M + \mathbf{H}_U \cdot \vec{\nabla} p_M \right). \end{aligned} \quad (53)$$

Equation (53) is equivalent to the isotropic (\vec{u}_M, p_M) -Biot formulation developed by Atalla et al.⁶¹

For a straightforward comparison with the conventional anisotropic Biot equations, it is rewritten in a (\vec{u}_M, \vec{U}_M) -formulation,⁶² as

$$\begin{aligned} \rho_{11} \cdot \ddot{\vec{u}}_M + \rho_{12} \cdot \ddot{\vec{U}}_M &= \vec{\nabla} \cdot \left({}^4\mathbf{C}_{11} : \vec{\nabla} \vec{u}_M + \mathbf{C}_{12} \vec{\nabla} \cdot \vec{U}_M \right), \\ \rho_{12}^T \cdot \ddot{\vec{u}}_M + \rho_{22} \cdot \ddot{\vec{U}}_M &= \vec{\nabla} \cdot \left(\mathbf{C}_{12}^T : \vec{\nabla} \vec{u}_M + C_{22} \vec{\nabla} \cdot \vec{U}_M \right). \end{aligned} \quad (54)$$

Note, that in Equation (54), the dissipative term proportional to the velocity is not included in accordance with the purely elastic approximation considered here. The inertial and elastic material properties of Biot’s model can then directly be expressed in terms of the homogenized coefficients:

$$\begin{cases} \rho_{11} = \mathbf{A}_\pi - \mathbf{H}_\pi \cdot \mathbf{H}_U^{-1} \cdot \mathbf{A}_U, \\ \rho_{22} = -\phi^2 \mathbf{H}_U^{-1}, \\ \rho_{12} = \phi \mathbf{H}_\pi \cdot \mathbf{H}_U^{-1}, \\ \rho_{12}^T = \phi \mathbf{H}_U^{-1} \cdot \mathbf{A}_U, \end{cases} \quad \begin{cases} {}^4\mathbf{C}_{11} = {}^4\mathbf{F}_\sigma - \frac{\mathbf{G}_\sigma \mathbf{B}_\epsilon}{C_\epsilon}, \\ C_{22} = -\frac{\phi^2}{C_\epsilon}, \\ \mathbf{C}_{12} = \frac{\phi \mathbf{G}_\sigma}{C_\epsilon}, \\ \mathbf{C}_{12}^T = \frac{\phi \mathbf{B}_\epsilon}{C_\epsilon}, \end{cases} \quad (55)$$

where for isotropic porous materials in Allard and Atalla,⁶³ tensor ${}^4\mathbf{C}_{11}$ corresponds to the material properties of the classic Biot theory P and N , that is, ${}^4\mathbf{C}_{11} = (P - 2N)\mathbf{II} + N({}^4\mathbf{I} + {}^4\mathbf{I}^{\text{RT}})$; \mathbf{C}_{12} corresponds to Q ; and C_{22} corresponds to R . Therefore, the proposed framework may also be used for obtaining anisotropic Biot’s coefficients for a microstructural unit cell with a saturated porous medium in the longwave regime.

4 | NUMERICAL EXAMPLES

4.1 | Unit cell

The selected numerical example is an epoxy honeycomb structure, with embedded composite resonators, saturated by air. Figure 2A shows the rectangular unit cell of width a_x and height a_y . The struts have a thickness of w and constrictions

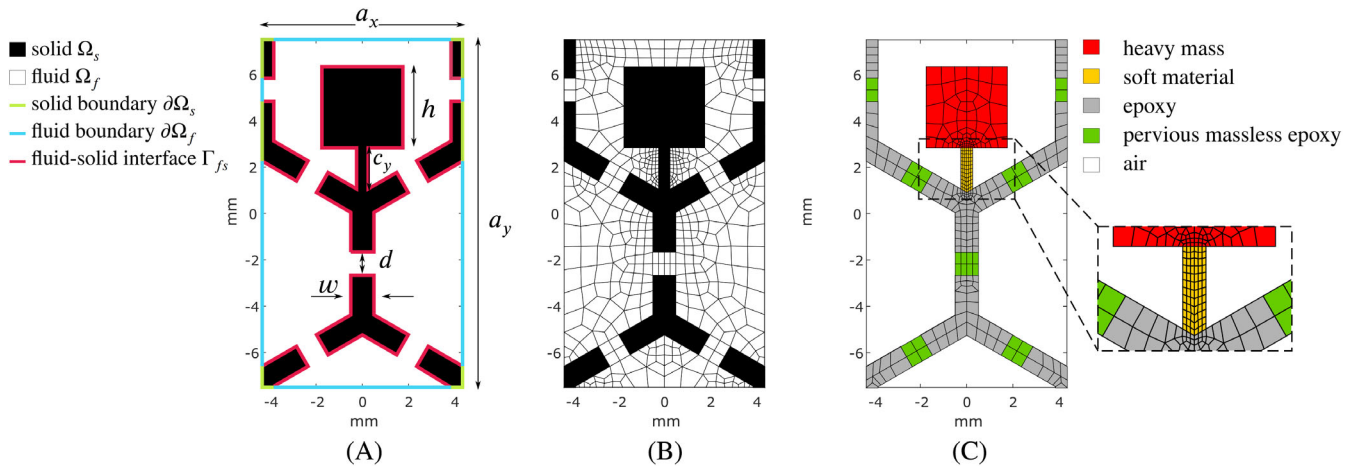


FIGURE 2 (A) 2D representative volume element depicting each phase and their respective boundaries (analogous to Figure 1C). (B) The finite element mesh of the fluid domain with elements colored in white. (C) The finite element mesh of the solid domain is colored according to the material properties: heavy mass (red), soft material (yellow), epoxy (gray), and pervious massless “epoxy” (green).

TABLE 2 The geometrical features of the unit cell depicted in Figure 2.

Feature	a_x	a_y	w	d	c_x	c_y	h
Value (mm)	8.66	15.0	1.00	1.00	0.5	1.78	3.50

TABLE 3 The material properties at ambient conditions of the materials in Figure 2.

Constituent	Property	Symbol	Value	Unit
Epoxy (solid host)	Mass density	ρ_s	11.8×10^2	kgm^{-3}
	Bulk modulus	K_s	4.54×10^9	Pa
	Shear modulus	G_s	1.31×10^9	Pa
Soft material (resonator)	Mass density	ρ_s	10.0×10^2	kgm^{-3}
	Bulk modulus	K_s	8.33×10^7	Pa
	Shear modulus	G_s	1.79×10^7	Pa
Heavy mass (resonator)	Mass density	ρ_s	11.6×10^2	kgm^{-3}
	Bulk modulus	K_s	5.23×10^{10}	Pa
	Shear modulus	G_s	1.49×10^{10}	Pa
Air (fluid host)	Mass density	ρ_f	1.23	kgm^{-3}
	Bulk modulus	K_f	1.44×10^5	Pa

of size d connecting the hexagonal pores. The cantilever has width (not shown in the figure) and height c_x and c_y , respectively, while the heavy mass is a square of size h . The numerical values of the geometric features are given in Table 2. The porosity $\phi = 0.727$ is the ratio of the fluid phase, indicated in white in Figure 2A, over the total volume of the representative volume element. The material properties of the different constituents in the unit cell are given in Table 3. The cantilever of the resonator is made from a relatively “soft” material, resulting in the subwavelength character of the low-frequency resonances.

Saturated porous materials typically have a solid skeleton with open pores, through which the fluid can flow freely. This requires both phases to be self-connected. This topological requirement imposes an intrinsically three-dimensional (3D) geometry. However, 3D geometries involve a large number of degrees of freedom. Since this work aims to illustrate

the proposed framework, a simplified 2D representation of the porous material is used instead, specifically designed to satisfy the self-connectivity of both phases. To this aim, the solid and the fluid meshes of the unit cell overlap at thin constrictions, see Figure 2. The fluid-structure interfaces are “deactivated” in these regions so the fluid can flow through the artificial green solid region. The added green elements are not accounted for in the computation of the porosity, they are massless and have the same elastic properties as epoxy, that is, the *host* solid. The existence of these elements ensures the connectivity of the solid phase. Since for the considered case here, no fluid resonance will be present, the fluid phase is considered here as part of the *host* domain for what concerns the separation of scales.

In Figure 2B,C, the finite element mesh used in the microscale simulation is shown. It has quadratic-serendipity elements for each phase, that is, the solid elements contain 8 nodes with 16 degrees of freedom for the nodal displacements (in 2D), whereas the fluid elements contain 8 nodes storing the nodal pressures. Moreover, plane strain is assumed for the solid phase.

Note that for the considered model, the honeycomb pore size is in the order of 10^{-2} m and its constrictions are of the order $d = 10^{-3}$ m. As pointed out by Biot,² for the features with the smallest characteristic length d , the inertial-dominated regime onsets for frequencies greater than $f_{\min} = 4\nu_{\text{air}}/(\pi d^2) \approx 20$ Hz, where ν_{air} is the kinematic viscosity of air at the ambient condition. Thus, it defines the lower-bound frequency f_{\min} for the longwave basis regime.

Considering multiple unit cells within one RVE is possible as long as the RVE has its boundaries lying within the host domain and the longwave approximation with respect to the supercell size holds (which will typically be violated at lower frequency compared to the single unit cell). However, it would introduce unnecessary additional computational costs, that is, more degrees of freedom at the microscale and additional local resonance modes from the supercell representation. Since the Bloch theorem states that wave propagation in a periodic medium may be fully described via a single-unit cell analysis within the reduced Brillouin zone, a supercell representation is unnecessary and not considered here.

4.2 | Homogenized material properties

The computational homogenization approach is applied to the considered unit cell. The effective material property coefficients of the longwave basis are computed from the (sub)matrices of the discretized unit cell model using expressions given in Appendix C. Thereafter, the homogenized material properties are converted in the form of the classic Biot coefficients with relations (55) and displayed in the Table 4.

The homogenized Biot coefficients are consistent with the positive-definiteness relation $\rho_{11} \cdot \rho_{22} - \rho_{12} \cdot \rho_{12}^T > 0$ and the negative reactive inertial coupling force that requires $\rho_{12} < 0$, as discussed in Biot.² In addition, the elastic stiffness tensor of the saturated solid ${}^4\mathbf{C}_{11}$ is one order of magnitude lower than the solid (epoxy) constituent, as expected since the high porosity ϕ causes a significant reduction in effective stiffness. Note the anisotropic character of the effective material properties due to the non-symmetry of the unit cell. For example, it is well known that hexagonal structures provide an

TABLE 4 Relevant homogenized material properties, in the form of the Biot coefficients (55), in the longwave regime of the unit cell shown in Figure 2.

Type	Symbol	Value	Unit
Porosity	ϕ	0.727	
Inertial (longwave) coefficients	ρ_{11}	$1304.0\vec{e}_1 \otimes \vec{e}_1 + 1303.8\vec{e}_2 \otimes \vec{e}_2$	kgm^{-3}
	ρ_{22}	$1.7215\vec{e}_1 \otimes \vec{e}_1 + 1.2257\vec{e}_2 \otimes \vec{e}_2$	kgm^{-3}
	ρ_{12}	$-0.6631\vec{e}_1 \otimes \vec{e}_1 - 0.6002\vec{e}_2 \otimes \vec{e}_2$	kgm^{-3}
Elastic (longwave) c oefficients	${}^4\mathbf{C}_{11}$	$(2.8992(\vec{e}_1 \otimes \vec{e}_1 \otimes \vec{e}_1 \otimes \vec{e}_1 + \vec{e}_2 \otimes \vec{e}_2 \otimes \vec{e}_2 \otimes \vec{e}_2) + 2.4902(\vec{e}_1 \otimes \vec{e}_1 \otimes \vec{e}_2 \otimes \vec{e}_2 + \vec{e}_2 \otimes \vec{e}_2 \otimes \vec{e}_1 \otimes \vec{e}_1) + 0.1999(\vec{e}_1 \otimes \vec{e}_2 \otimes \vec{e}_2 \otimes \vec{e}_1 + \vec{e}_1 \otimes \vec{e}_2 \otimes \vec{e}_1 \otimes \vec{e}_2 + \vec{e}_2 \otimes \vec{e}_1 \otimes \vec{e}_2 \otimes \vec{e}_1 + \vec{e}_2 \otimes \vec{e}_1 \otimes \vec{e}_1 \otimes \vec{e}_2)) \times 10^8$	Pa
	C_{22}	1.0480×10^5	Pa
	\mathbf{C}_{12}	$(4.3244\vec{e}_1 \otimes \vec{e}_1 + 1.0416\vec{e}_2 \otimes \vec{e}_2) \times 10^4$	Pa

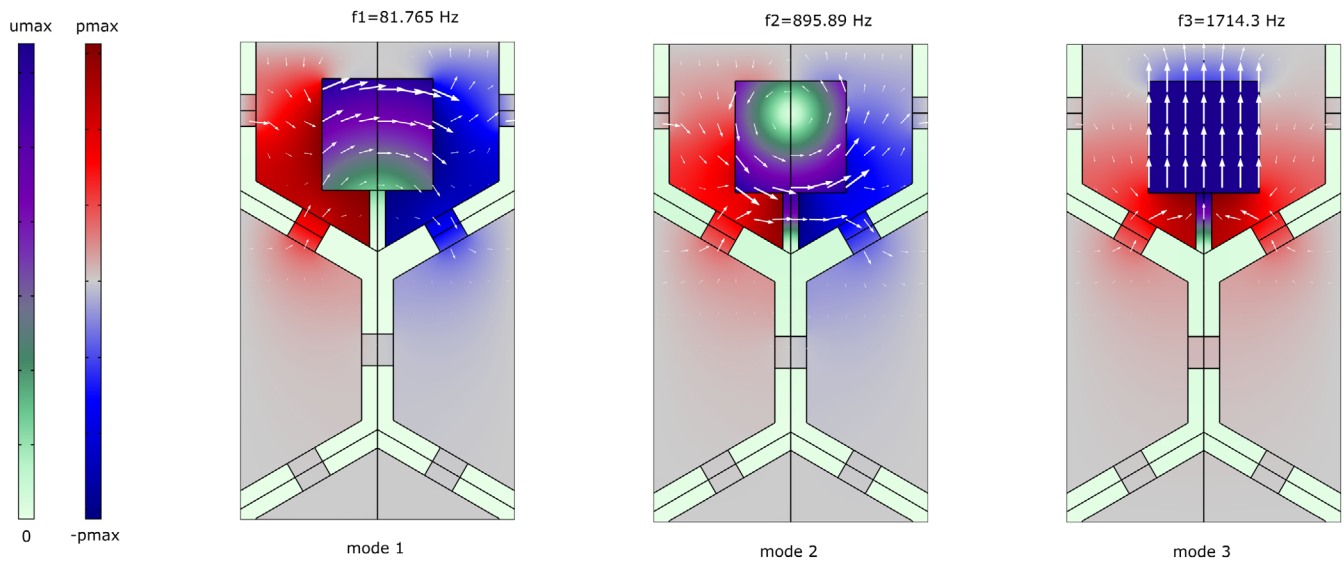


FIGURE 3 Three lowest modes $j = 1, 2, 3$ ($Q = 3$) of the time-harmonic boundary value problem (33). The primary field variables are plotted in the reference configuration. White arrows show the direction and magnitude of the displacements.

TABLE 5 Relevant homogenized material properties in the local resonance regime. Resonant modes shown in Figure 3.

Type	Symbol	Value	Unit
Eigenfrequencies $f_j = \frac{\omega_j}{2\pi}$	f_1	81.765	Hz
	f_2	895.89	Hz
	f_3	1714.3	Hz
Solid-phase momentum enrichment \vec{a}	\vec{a}_1	$76.67\vec{e}_1$	kg m^{-2}
	\vec{a}_2	$-4.838\vec{e}_1$	kg m^{-2}
	\vec{a}_3	$-4.756\vec{e}_2$	kg m^{-2}
Evolution equation coefficient $\vec{\alpha}$	$\vec{\alpha}_1$	$11.25 \vec{e}_1$	kg m
	$\vec{\alpha}_2$	$-50.28 \vec{e}_1$	kg m
	$\vec{\alpha}_3$	$-232.3 \vec{e}_2$	kg m

isotropic effective stiffness, and indeed this property is verified for the solid phase stiffness tensor in vacuum ${}^4\mathbf{F}_\sigma$ (not shown). Once ${}^4\mathbf{F}_\sigma$ is converted to ${}^4\mathbf{C}_{11}$, that is, the saturated solid phase stiffness tensor, the isotropy is broken since it depends also on the anisotropic coupling coefficients \mathbf{G}_σ and \mathbf{B}_e (not shown). The anisotropic coupling emerges from the lack of symmetry in x and y directions.

The three considered lowest mode shapes of the time-harmonic boundary value problem (33) are depicted in Figure 3. It has been verified with a dispersion analysis that these 3 modes are indeed fully localized and thus comply with the superposition (34). The fourth mode $f_4 = 7604.2$ Hz (not shown) has a significant displacement at the boundary of the *host* solid, indicating that it is not localized. Thus, the superposition of “local resonance” with “longwave” response is no longer valid and the homogenization framework is not applicable in this regime.

Since these three dipolar modes are involved in the solid phase resonance, only the material properties enriching the solid phase momentum, shown in Table 5, assume significant values. The other local resonance material properties have a negligible contribution to the wave propagation as shown in Appendix D. For a wave propagating in the x direction, the first two modes with frequencies f_1 and f_2 , will interact with compression waves given their pronounced amplitude in the x direction while the third mode f_3 will interact with shear waves.

4.3 | Dispersion analysis

The dispersion properties of the homogenized continuum are investigated assuming that the primary fields are time- and space-harmonic, that is, taking the plane wave form

$$(\vec{u}_M, p_M, \eta_Q) = (\hat{\vec{u}}_M, \hat{p}_M, \hat{\eta}_Q) e^{(+i\omega t - i\vec{k} \cdot \vec{x}_M)} \quad (56)$$

which can be inserted into the governing Equation (49). Taking into account the constitutive relations including only the relevant coefficients listed in tables 4 and 5, here referred to as homogenized enriched Biot continuum, yields an eigenvalue problem of size $2 + 1 + Q$ in 2D (resp. $3 + 1 + Q$ in 3D). Expressing the sums in Equation (47) in matrix format, for example, $\sum_{j=1}^Q \vec{a}_j \cdot \vec{\eta}_j = \vec{a}^T \cdot \vec{\eta}_Q$ for a compact notation, the following eigenvalue problem is obtained

$$\left(\begin{array}{c} \left(\begin{array}{ccc} \mathbf{A}_\pi & \vec{0} & \vec{a}^T \\ (-\omega^2) \left[\begin{array}{ccc} i(-\mathbf{B}_e \cdot \vec{k} + \vec{k} \cdot \mathbf{A}_U) & C_e & \vec{0}_Q^T \\ \vec{a} & 0_Q & \mathbf{I}_{QQ}^{(lr)} \end{array} \right] \end{array} \right) + \left[\begin{array}{ccc} \vec{k} \cdot \mathbf{F}_\sigma^{LT} \cdot \vec{k} & i(-\mathbf{H}_\pi \cdot \vec{k} + \vec{k} \cdot \mathbf{G}_\sigma^T) & \vec{0}_Q^T \\ \vec{0} & \vec{k} \cdot \mathbf{H}_U \cdot \vec{k} & \vec{0}_Q^T \\ \vec{0}_Q & \vec{0}_Q & \mathbf{I}_{QQ}^{(lr)} \end{array} \right] \end{array} \right) \begin{pmatrix} \hat{\vec{u}}_M \\ \hat{p}_M \\ \hat{\eta}_Q \end{pmatrix} = \begin{pmatrix} \vec{0} \\ 0 \\ 0 \end{pmatrix}, \quad (57)$$

where $\mathbf{I}_{QQ}^{(lr)}$ and $\mathbf{I}_{QQ}^{(lr)}$ are the matrices defined in (39) and (40). For periodic media, for a given real-valued wavevector \vec{k} spanning the irreducible Brillouin zone, the corresponding eigenvalue ω^2 and eigenvector $[\hat{\vec{u}}_M \ \hat{p}_M \ \hat{\eta}_Q]^T$ can be obtained by solving (57). As an example, the case $\vec{k} = k\vec{e}_x$ is considered with $k \in [0, \frac{\pi}{a_x}]$, where a_x is the unit cell size in the x direction, see Figure 2. The same analysis can be carried out in other directions of interest; for instance, the propagation y direction is different from the x direction because of the asymmetry of the unit cell. In the following, $\omega(k_x)$ -curves will be shown up to the frequency of $f_{\max} \approx 1600$ Hz which is the approximated upper-bound frequency for the longwave basis validity. As shown in Appendix D, the valid frequency range of the proposed homogenized model is estimated to be $[f_{\min}, f_{\max}] = [20, 1600]$ Hz.

The computed dispersion curves of the homogenized continuum are shown in Figure 4. To assess the validity of the results, as the reference solution for the dispersion spectrum, a direct numerical simulation of the unit cell is performed by applying Bloch-Floquet periodic boundary conditions also shown in Figure 4. This direct numerical simulation Bloch analysis involved $2(b+i) + (b'+i') = 2B + I \approx 2000$ degrees of freedom compared to $2 + 1 + Q = 6$ for the online stage of the homogenization approach.

Excellent correspondence is observed between the dispersion spectrum of the homogenized continuum and the reference Bloch solution.

To identify the nature of the dispersion branches, the wave polarization and propagating phase (that is, solid or fluid) have been identified. In Figure 4A, the polarization ratio is computed for the DNS and the homogenized solutions according to:

$$\text{DNS polarization ratio} = \frac{\int_{\Omega_s^{(host)}} \|\vec{u} \cdot \vec{k}\|}{\int_{\Omega_s^{(host)}} \|\vec{u}\| \|\vec{k}\|}, \quad \text{Hom. polarization ratio} = \frac{\|\hat{\vec{u}}_M \cdot \vec{k}\|}{\|\hat{\vec{u}}_M\| \|\vec{k}\|}. \quad (58)$$

For the DNS, the homogenized solid displacement \vec{u} in the direction of propagation is averaged over the *host* solid domain $\Omega_s^{(host)}$, while for the enriched Biot continuum the displacement component of the eigenvector $[\hat{\vec{u}}_M \ \hat{p}_M \ \hat{\eta}_Q]^T$ is taken of the problem (57). Similarly, the phase-born ratio, plotted in Figure 4B, is obtained as

$$\text{DNS ratio} = \log_{10} \left(\frac{\int_{\Omega_f} \|\ddot{\vec{U}} = -1/\rho_f \vec{\nabla} p\|}{\int_{\Omega_s^{(host)}} \omega^2 \|\vec{u}\|} \right), \quad \text{Hom. ratio} = \log_{10} \left(\frac{\|\ddot{\vec{U}}_M = (-\omega^2 \mathbf{A}_U \cdot \hat{\vec{u}}_M + \mathbf{H}_U \cdot \vec{\nabla} \hat{p}_M)/\phi\|}{\omega^2 \|\hat{\vec{u}}_M\|} \right). \quad (59)$$

Considering the dispersion spectrum of the considered saturated porous material, 3 dispersion curves are distinguished in the longwave regime; two solid-born waves that can be categorized as compression and shear waves according to their polarization and one fluid-born branch.

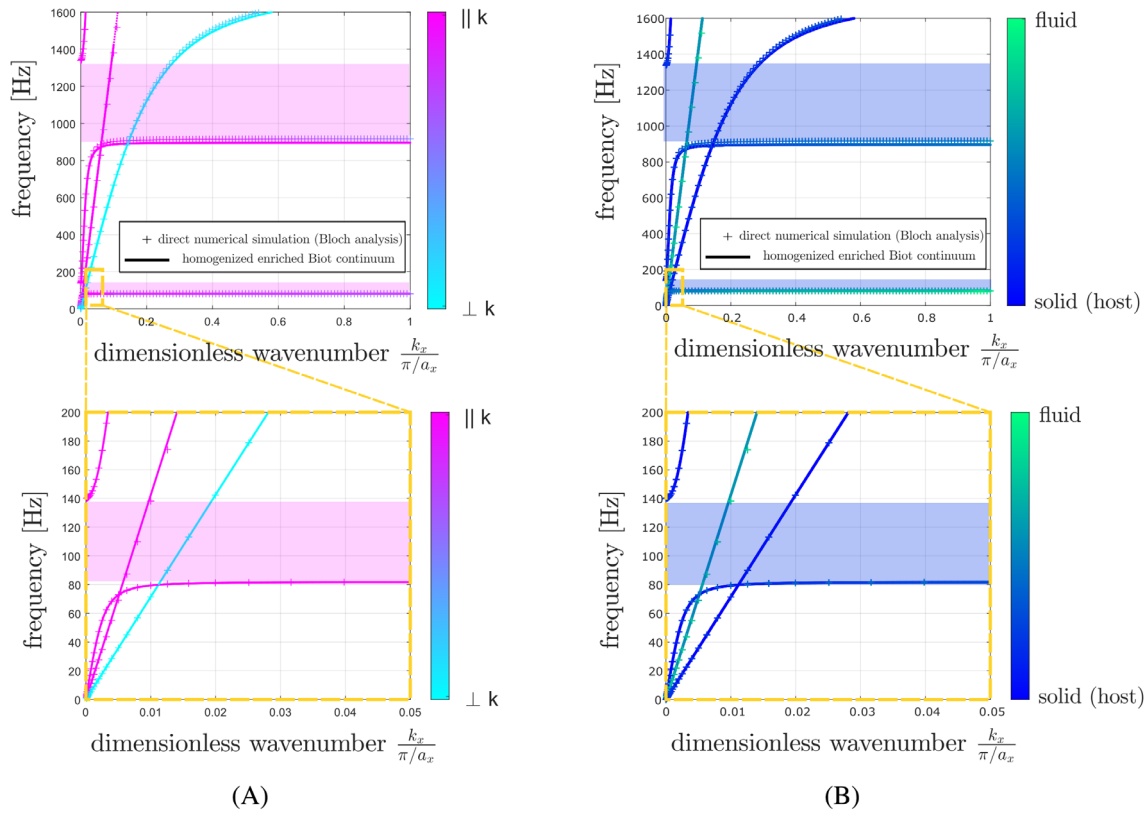


FIGURE 4 Dispersion curves obtained via the computational homogenization approach (solid line —) versus the dispersion curves computed using the direct numerical simulation Bloch Analysis (+). The color bar shows (A) the polarization of the host solid medium and (B) the preferential phase for each propagating mode. The bottom figures are zoomed windows in the low-frequency corner.

As can be seen from bottom Figure 4A,B, the solid-born compression branch becomes dispersive at small dimensionless wavenumber and becomes flat, evidencing that the local resonance mode becomes active. This opens the partial bandgap, shaded in Figure 4. Similar observations hold for the second compressive solid branch that opens the second partial bandgap. All these effects are excellently captured by the homogenized enriched Biot continuum description.

The solid phase effective density of the enriched Biot continuum can be calculated by assuming a time-harmonic solution, inserting Equation (48) into the solid phase momentum Equation (first equation of (50)) thus eliminating the η_j variables, giving

$$\mathbf{A}_\pi^{(\text{eff})}(\omega) = \mathbf{A}_\pi + \sum_{j=1}^Q \frac{\omega^2}{-\omega^2 + \omega_j^2} \vec{a}_j \otimes \vec{a}_j \quad (60)$$

that becomes sharply negative when the propagating frequency approaches $\omega \rightarrow \omega_j^+$. This is indeed a characteristic feature of a locally resonant metamaterial (LRAM), as originally introduced by Liu.⁶⁴ In the present work, only the resonator in the solid phase is considered. If resonance occurs in the fluid phase, the partial bandgap would occur for the fluid-born branch, for example, for the metamaterial design shown by Cheng et al.,⁶⁵ and later in the works.^{66,67} Application of the proposed framework to fluid phase resonance will be presented in a forthcoming work.

Finally, it is remarked for the numerical examples, shown in the Appendix D, that, at least for the unit cell considered in this work, the dispersion behavior in the x direction of the homogenized continuum including all longwave coefficients defined in (47) is essentially the same as including only Biot's coefficients (51) (in addition to the relevant local resonance coefficients (52) which are $(\vec{a}, \vec{\alpha})$ for this unit cell) yielding an effective enriched Biot continuum. The generality of this conclusion will still need to be investigated and it will be the subject of future work.

4.4 | Wave transmission through a sandwiched porous layer

Next, transmission through a porous metamaterial layer is considered. For assessing the response of the homogenized continuum in a finite-sized domain the setup shown in Figure 5 is used. The wave excitation is a plane wave impinging from a plain-air acoustic domain onto the porous layer sandwiched between two thin solid layers. The purpose of adding a thin solid will be motivated in the next paragraph. The porous layer is made of a collection of 10 unit cells sequentially arranged in the x direction. Periodic boundary conditions are imposed on the top and bottom surfaces to mimic an infinite layer in the y direction. Perfectly matched layers (PML) domains are used to mimic an infinite incoming and outgoing acoustic domain in the x direction. The reference direct numerical simulation solution is computed by solving the full-field fluid-structure problem depicted in Figure 5A.

The homogenized response is computed with the model depicted in Figure 5B that combines a fluid (acoustic) domain in a p_a -formulation, a solid domain in a \bar{u}_a -formulation, and the homogenized enriched Biot domain. The subscript a indicates the domains that are not homogenized. The homogenized domain is described by the discretized weak form of Equation (49) with the constitutive relations including the coefficients of tables 4 and 5, implemented in COMSOL using the Weak Form PDE interface in the mathematics module. The coupling between the enriched Biot and solid is given imposing continuity of total tractions, continuity of normal solid displacement, and no fluid mass flux across the boundary, as defined in Atalla and Sgard⁶⁸

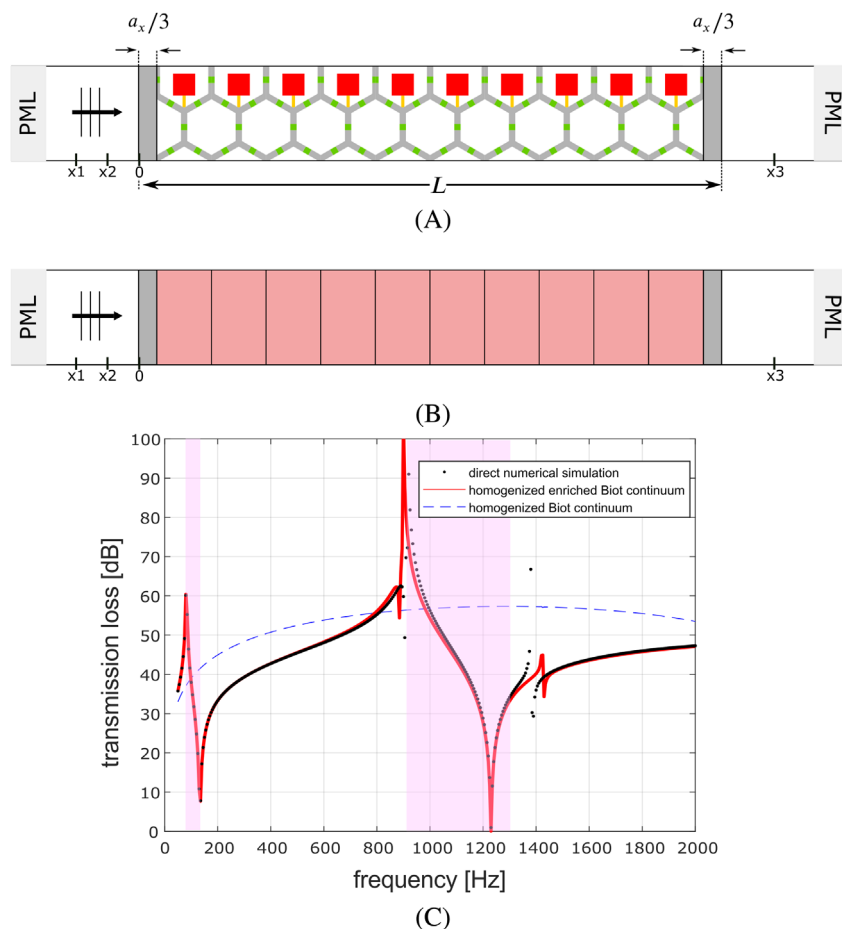


FIGURE 5 (A) Full-field fluid-structure interaction model. (B) Equivalent macroscopic model where the porous layer is treated as a homogenized continuum. The mesh is shown only in the homogenized domain. (C) The transmission loss curve computed via the three-microphone method for models (A) and (B).

$$\begin{aligned}
((1 - \phi)\sigma_M + \phi(-p_M \mathbf{I})) \cdot \vec{n} &= \sigma_a \cdot \vec{n}, \\
\vec{u}_M \cdot \vec{n} &= \vec{u}_a \cdot \vec{n}, \\
(\vec{u}_M - \vec{U}_M) \cdot \vec{n} &= \vec{0},
\end{aligned} \tag{61}$$

where \vec{n} is the normal to the solid-enriched Biot interface. The mesh of the enriched Biot continuum, shown in Figure 5B, has quadratic serendipity elements with the size of the unit cell.

The dispersion curves of Figure 4C show that the bandgap occurs only for the compression solid-born branches, whereas fluid-born and shear solid-born branches can still transmit the acoustic wave through the porous layer in the considered frequency range. However, since the plane wave motion occurs in the x direction, the shear solid-born branch is not excited. On the other hand, the presence of the solid layers before and after the porous layer drastically reduces the energy transmission through the fluid-born branch, forcing the transmitted energy to pass through the solid branch. As a consequence, the proposed setup is a good candidate to validate the enriched homogenized continuum in a finite-sized case since the transmission will occur mainly through the highly dispersive compression solid-born branch. Note, that despite being named “solid-born branch” fluid motion still occurs since the Bloch mode shapes are a fully coupled fluid-structure interaction unit cell problem.

For the sake of reducing computational costs, time-harmonicity of the primary fields is assumed, yielding a frequency domain problem that characterizes the wave response after an infinitely long period. Note, that time-harmonicity is optional and the transient response of a homogenized enriched Biot continuum can be obtained using a standard time-integration scheme. Following the approach by Lewinska et al.,^{34,69} a three-microphone method is used for computing the transmission loss through the sandwiched layer. For a given excitation frequency ω , the complex pressure amplitudes p_1 , p_2 , and p_3 are obtained as the average pressure $p(\vec{x}, \omega)$ on a vertical line at positions x_1 , x_2 , and x_3 , respectively, indicated in Figure 5A,B. The calculation of the reflection and transmission coefficients, followed by the calculation of the transmission loss, is performed using the expressions

$$\begin{cases} R(\omega) = \frac{p_2 e^{-ik^{(air)}x_1} - p_1 e^{-ik^{(air)}x_2}}{p_1 e^{ik^{(air)}x_2} - p_2 e^{ik^{(air)}x_1}}, \\ T(\omega) = \frac{p_3 (e^{-ik^{(air)}x_2} + R(\omega)e^{ik^{(air)}x_2})}{p_2 e^{-ik^{(air)}x_3}} e^{-ik^{(air)}L}, \end{cases} \quad \text{and} \quad TL(\omega) = 20 \log_{10} \left(\frac{1}{\|T(\omega)\|} \right), \tag{62}$$

where $L = (10 + 2/3)a_x$ is the total layer thickness, and $k^{(air)} = \omega/\sqrt{K_f/\rho_f}$ is the wavenumber in the plain-air acoustic domain.

The transmission loss computed with the direct numerical simulation and the homogenized enriched Biot continuum is compared in Figure 5C. An excellent agreement can be observed up to 1300 Hz when the homogenized continuum response starts to deviate from the reference DNS solution. As discussed in Wamsler⁷⁰ in the context of component mode synthesis of structures, the mode-based model reduction technique, similar to the one used in Section 3.2, adequately approximates the full dynamics of the component up to half the frequency of the truncated mode. that is, $f_3/2 \approx 800$ Hz for the considered case. Additionally, in Figure 5C, the Biot continuum computed via the longwave basis only, that is, disregarding the contribution of the local resonance, is not capable of capturing the full-field transmission loss illustrating the need for the inclusion of the internal dynamics via the local resonance basis. The number of degrees of freedom solved for the model depicted in Figure 5A was around 53,000, while, the model including the homogenized continuum of Figure 5B, was around 750, that is, a reduction of approximately 98%.

5 | CONCLUSION

The demanding computational efforts of models addressing the dynamic response of heterogeneous porous materials are rooted in their fine geometrical features and constituents. Multiscale approaches propose surrogate models as an alternative for computing the constitutive response of such materials with a systematic approach. Computational homogenization proves to be a versatile multiscale method for upscaling general microscopic descriptions with only a

few macroscale assumptions, and, when combined with model reduction techniques, considerably saves computational resources at the expense of sacrificing generality.

In this article, a multiscale model is proposed for solving transient wave propagation in porous materials. The microscale is governed by a conventional linear fluid-structure interaction problem, where the solid is treated as elastic and the fluid is inviscid and compressible on a quiescent background. The macro and microscales are coupled in a variationally consistent way employing an extended form of the Hill-Mandel principle that also includes the inertial terms. The method is based on the relaxed separation of scales, where only the boundary of the RVE is required to be in a long wavelength regime. With this assumption, the constructed reduced space combines the longwave response and the local resonance response, represented by a truncated number of resonant modes, leading to a macroscopic homogenized enriched continuum where the inertia from the microscale is captured, at the macroscale, through a set of emerging internal variables. It is important to emphasize that the microscale dynamics is limited to the case where it is localized within the representative volume element.

A fluid-saturated porous solid LRAM is used to demonstrate the proposed framework. Efficacy and accuracy were observed for an air-saturated porous honeycomb structure with embedded resonators. The macroscale model greatly reduces the number of degrees of freedom compared to the full-field problem, allowing the use of a coarse mesh relative to the real size of the pore.

The upscaled constitutive model presented in this article is versatile, allowing for non-standard macroscopic responses according to the defined RVE. For the considered numerical example, the dispersion relation shows that the effective continuum behaves as an extended Biot model enriched with internal variables related to the mode contributions. Further investigation on the influence of the non-standard constitutive terms deserves investigation. Moreover, extension of the framework to include dissipation will be presented in the future work.

ACKNOWLEDGMENTS

This publication is part of the project SUBMETA with project number 17884 of the research program “Materials NL: Challenges 2018” which is (partly) financed by the Dutch Research Council (NWO).

CONFLICT OF INTEREST

The authors declare no potential conflict of interest.

DATA AVAILABILITY STATEMENT

The code (MATLAB script) and COMSOL models supporting this article, Liupekevicius et al.,⁷¹ have been uploaded to the external repository 4TU.ResearchData with DOI <https://data.4tu.nl/datasets/f422cac5-b959-445d-9e2b-ad4067ee9580>.

ORCID

Renan Liupekevicius  <https://orcid.org/0000-0003-4517-3899>

Varvara G. Kouznetsova  <https://orcid.org/0000-0003-0113-6471>

REFERENCES

1. Milton GW, Willis JR. On modifications of Newton's second law and linear continuum elastodynamics. *Proc R Soc A*. 2007;463(2079):855-880.
2. Biot MA. Theory of propagation of elastic waves in a fluid-saturated porous solid. II. Higher frequency range. *J Acoust Soc Am*. 1956;28(2):179-191.
3. Serpieri R, Della Corte A, Travascio F, Rosati L. Variational theories of two-phase continuum poroelastic mixtures: a short survey. *General Contin Models Classical Adv Mat*. 2016;42:377-394.
4. Bedford A, Drumheller DS. Theories of immiscible and structured mixtures. *Int J Eng Sci*. 1983;21(8):863-960.
5. Bedford A. *Hamilton's Principle in Continuum Mechanics*. 139. Pitman Advanced Publishing Program Boston; 1985.
6. Burridge R, Keller JB. Poroelasticity equations derived from microstructure. *J Acoust Soc Am*. 1981;70(4):1140-1146.
7. Whitaker S. Flow in porous media I: a theoretical derivation of Darcy's law. *Transp Porous Media*. 1986;1:3-25.
8. Pride SR, Gangi AF, Morgan FD. Deriving the equations of motion for porous isotropic media. *J Acoust Soc Am*. 1992;92(6):3278-3290.
9. Geers MGD, Kouznetsova VG, Brekelmans WAM. Multi-scale computational homogenization: trends and challenges. *J Comput Appl Math*. 2010;234(7):2175-2182.
10. Geers MGD, Kouznetsova VG, Matouš K, Yvonnet J. Homogenization methods and multiscale modeling: nonlinear problems. *Encyclopedia of Computational Mechanics*. 2nd ed.; Wiley; 2017:1-34.
11. Matouš K, Geers MGD, Kouznetsova VG, Gillman A. A review of predictive nonlinear theories for multiscale modeling of heterogeneous materials. *J Comput Phys*. 2017;330:192-220.

12. Özdemir I, Brekelmans WAM, Geers MGD. Computational homogenization for heat conduction in heterogeneous solids. *Int J Numer Methods Eng*. 2008;73(2):185-204.
13. Larsson F, Runesson K, Su F. Computational homogenization of uncoupled consolidation in micro-heterogeneous porous media. *Int J Numer Anal Methods Geomech*. 2010;34(14):1431-1458.
14. Su F, Larsson F, Runesson K. Computational homogenization of coupled consolidation problems in micro-heterogeneous porous media. *Int J Numer Methods Eng*. 2011;88(11):1198-1218.
15. Jänicke R, Quintal B, Steeb H. Numerical homogenization of mesoscopic loss in poroelastic media. *Eur J Mech A Solids*. 2015;49:382-395.
16. Jänicke R, Larsson F, Runesson K, Steeb H. Numerical identification of a viscoelastic substitute model for heterogeneous poroelastic media by a reduced order homogenization approach. *Comput Methods Appl Mech Eng*. 2016;298:108-120.
17. Quintal B, Jänicke R, Rubino JG, Steeb H, Holliger K. Sensitivity of S-wave attenuation to the connectivity of fractures in fluid-saturated rocks. *Geophysics*. 2014;79(5):WB15-WB24.
18. Jänicke R, Larsson F, Runesson K. A poro-viscoelastic substitute model of fine-scale poroelasticity obtained from homogenization and numerical model reduction. *Comput Mech*. 2020;65(4):1063-1083.
19. Sandström C, Larsson F, Runesson K, Johansson H. A two-scale finite element formulation of stokes flow in porous media. *Comput Methods Appl Mech Eng*. 2013;261:96-104.
20. Sandstrom C, Larsson F. Variationally consistent homogenization of stokes flow in porous media. *Int J Multiscale Comput Eng*. 2013;11(2):117-138.
21. Sandström C, Larsson F, Runesson K. Homogenization of coupled flow and deformation in a porous material. *Comput Methods Appl Mech Eng*. 2016;308:535-551.
22. Gao K, Van Dommelen JAW, Göransson P, Geers MGD. A homogenization approach for characterization of the fluid-solid coupling parameters in Biot's equations for acoustic poroelastic materials. *J Sound Vib*. 2015;351:251-267.
23. Gao K, van JAW, Göransson P, Geers MGD. Computational homogenization of sound propagation in a deformable porous material including microscale viscous-thermal effects. *J Sound Vib*. 2016;365:119-133.
24. Fellah ZEA, Depollier C. Transient acoustic wave propagation in rigid porous media: a time-domain approach. *J Acoust Soc Am*. 2000;107(2):683-688.
25. Perrot C, Chevillotte F, Tan Hoang M, et al. Microstructure, transport, and acoustic properties of open-cell foam samples: experiments and three-dimensional numerical simulations. *J Appl Phys*. 2012;111(1):1-16.
26. Zieliński TG, Venegas R, Perrot C, Červenka M, Chevillotte F, Attenborough K. Benchmarks for microstructure-based modelling of sound absorbing rigid-frame porous media. *J Sound Vib*. 2020;483:115441.
27. Bedford A, Drumheller DS. A variational theory of porous media. *Int J Solids Struct*. 1979;15(12):967-980.
28. Smeulders DMJ, Van Dongen MEH. Wave propagation in porous media containing a dilute gas-liquid mixture: theory and experiments. *J Fluid Mech*. 1997;343:351-373.
29. Frehner M, Steeb H, Schmalholz SM, Petrin A. Wave velocity dispersion and attenuation in media exhibiting internal oscillations. *Wave Propagation in Materials for Modern Applications*. In-Tech Education and Publishing; 2010:455-476.
30. Steeb H, Kurzeja PS, Frehner M, Schmalholz SM. Phase velocity dispersion and attenuation of seismic waves due to trapped fluids in residual saturated porous media. *Vadose Zone J*. 2012;11(3):vzj2011-0121.
31. Steeb H, Kurzeja PS, Schmalholz SM. Wave propagation in unsaturated porous media. *Acta Mech*. 2014;225(8):2435-2448.
32. Kurzeja P, Steeb H. Acoustic waves in saturated porous media with gas bubbles. *Philos Trans R Soc A*. 2022;380(2237):20210370.
33. Venegas R, Boutin C. Acoustics of permeo-elastic materials. *J Fluid Mech*. 2017;828:135-174.
34. Lewińska MA, Kouznetsova VG, Van Dommelen JAW, Geers MGD. Computational homogenisation of acoustic metafoams. *Eur J Mech A Solids*. 2019;77:103805.
35. Lewińska MA, Van Dommelen JAW, Kouznetsova VG, Geers MGD. Broadening the attenuation range of acoustic metafoams through graded microstructures. *J Sound Vib*. 2020;483:115472.
36. Khoei AR, Hajiabadi MR. Fully coupled hydromechanical multiscale model with microdynamic effects. *Int J Numer Methods Eng*. 2018;115(3):293-327.
37. Wu W, Yang Y, Zheng H, Zhang L, Zhang N. Numerical manifold computational homogenization for hydro-dynamic analysis of discontinuous heterogeneous porous media. *Comput Methods Appl Mech Eng*. 2022;388:114254.
38. Auriault JL, Boutin C. Long wavelength inner-resonance cut-off frequencies in elastic composite materials. *Int J Solids Struct*. 2012;49(23-24):3269-3281.
39. Pham K, Kouznetsova VG, Geers MGD. Transient computational homogenization for heterogeneous materials under dynamic excitation. *J Mech Phys Solids*. 2013;61(11):2125-2146.
40. Van Nuland TFW, Silva PB, Sridhar A, Geers MGD, Kouznetsova VG. Transient analysis of nonlinear locally resonant metamaterials via computational homogenization. *Math Mech Solids*. 2019;24(10):3136-3155.
41. Sridhar A, Kouznetsova VG, Geers MGD. Homogenization of locally resonant acoustic metamaterials towards an emergent enriched continuum. *CComput Mech*. 2016;57:423-435.
42. Sridhar A, Kouznetsova VG, Geers MGD. A semi-analytical approach towards plane wave analysis of local resonance metamaterials using a multiscale enriched continuum description. *Int J Mech Sci*. 2017;133:188-198.
43. Sridhar A, Liu L, Kouznetsova VG, Geers MGD. Homogenized enriched continuum analysis of acoustic metamaterials with negative stiffness and double negative effects. *J Mech Phys Solids*. 2018;119:104-117.
44. Liu L, Sridhar A, Geers MGD, Kouznetsova VG. Computational homogenization of locally resonant acoustic metamaterial panels towards enriched continuum beam/shell structures. *Comput Methods Appl Mech Eng*. 2021;387:114161.

45. Blanco PJ, Sánchez PJ, De Souza Neto EA, Feijóo RA. Variational foundations and generalized unified theory of RVE-based multiscale models. *Arch Comput Methods Eng*. 2016;23:191-253.
46. Roca D, Lloberas-Valls O, Cante J, Oliver J. A computational multiscale homogenization framework accounting for inertial effects: application to acoustic metamaterials modelling. *Comput Methods Appl Mech Eng*. 2018;330:415-446.
47. De Souza Neto EA, Blanco PJ, Sánchez PJ, Feijóo RA. An RVE-based multiscale theory of solids with micro-scale inertia and body force effects. *Mech Mater*. 2015;80:136-144.
48. Kouznetsova VG, Brekelmans WAM, Baaijens FPT. An approach to micro-macro modeling of heterogeneous materials. *Ccomput Mech*. 2001;27(1):37-48.
49. Terada K, Hori M, Kyoya T, Kikuchi N. Simulation of the multi-scale convergence in computational homogenization approaches. *Int J Solids Struct*. 2000;37(16):2285-2311.
50. Molinari A, Mercier S. Micromechanical modelling of porous materials under dynamic loading. *J Mech Phys Solids*. 2001;49(7):1497-1516.
51. Zienkiewicz OC, Taylor RL, Zhu JZ. *The Finite Element Method: its Basis and Fundamentals*. Elsevier; 2005.
52. Marburg S, Nolte B. *Computational Acoustics of Noise Propagation in Fluids: Finite and Boundary Element Methods*. Springer; 2008:578.
53. Sandberg G. A new strategy for solving fluid-structure problems. *Int J Numer Methods Eng*. 1995;38(3):357-370.
54. Morand HJP, Ohayon R. *Fluid Structure Interaction: Applied Numerical Methods*. John Wiley & Sons; 1995.
55. Wandinger J. A symmetric Craig-Bampton method of coupled fluid-structure systems. *Eng Comput*. 1998;15(4):450-461.
56. Sandberg G, Hansson PA, Gustavsson M. Domain decomposition in acoustic and structure-acoustic analysis. *Comput Methods Appl Mech Eng*. 2001;190(24-25):2979-2988.
57. Davidsson P. *Structure-Acoustic Analysis; Finite Element Modelling and Reduction Methods*. PhD thesis. Lund University; 2004.
58. Maess M, Gaul L. Substructuring and model reduction of pipe components interacting with acoustic fluids. *Mech Syst Signal Process*. 2006;20(1):45-64.
59. Nassar H, He QC, Auffray N. Willis elastodynamic homogenization theory revisited for periodic media. *J Mech Phys Solids*. 2015;77:158-178.
60. Nassar H, Yousefzadeh B, Fleury R, et al. Nonreciprocity in acoustic and elastic materials. *Nat Rev Mater*. 2020;5(9):667-685.
61. Atalla N, Panneton R, Debergue P. A mixed displacement-pressure formulation for poroelastic materials. *J Acoust Soc Am*. 1998;104(3):1444-1452.
62. Biot MA. Generalized theory of acoustic propagation in porous dissipative media. *J Acoust Soc Am*. 1962;34(9A):1254-1264.
63. Allard J, Atalla N. *Propagation of Sound in Porous Media: Modelling Sound Absorbing Materials*. John Wiley & Sons; 2009.
64. Liu Z, Zhang X, Mao Y, et al. Locally resonant sonic materials. *Science*. 2000;289(5485):1734-1736.
65. Cheng Y, Zhou C, Yuan BG, Wu DJ, Wei Q, Liu XJ. Ultra-sparse metasurface for high reflection of low-frequency sound based on artificial Mie resonances. *Nat Mater*. 2015;14(10):1013-1019.
66. Miniaci M, Krushynska A, Movchan AB, Bosia F, Pugno NM. Spider web-inspired acoustic metamaterials. *Appl Phys Lett*. 2016;109(7):1-4.
67. Man X, Liu T, Xia B, Luo Z, Xie L, Liu J. Space-coiling fractal metamaterial with multi-bandgaps on subwavelength scale. *J Sound Vib*. 2018;423:322-339.
68. Atalla N, Sgard F. *Finite Element and Boundary Methods in Structural Acoustics and Vibration*. CRC Press; 2015.
69. Lewińska MA, Van Dommelen JAW, Kouznetsova VG, Geers MGD. Towards acoustic metafoams: the enhanced performance of a poroelastic material with local resonators. *J Mech Phys Solids*. 2019;124:189-205.
70. Wamsler M. On the selection of the mode cut-off number in component mode reduction. *Eng Comput*. 2009;25(2):139-146.
71. Liupekevičius R, Van Dommelen JAW, Geers MGD, Kouznetsova VG. MATLAB script and COMSOL models of the article 'Transient computational homogenization of heterogeneous poroelastic media with local resonances' [Internet]. 4TU.ResearchData 2024 Available from: <https://data.4tu.nl/datasets/f422cac5-b959-445d-9e2b-ad4067ee9580/1>
72. Goldstein ME. *Aeroacoustics*. McGraw-Hill; 1976.
73. Landau LD, Lifshitz EM. *Course of Theoretical Physics*. Elsevier; 2013.
74. Willis JR. Effective constitutive relations for waves in composites and metamaterials. *Proc R Soc A*. 2011;467(2131):1865-1879.

How to cite this article: Liupekevičius R, van Dommelen JAW, Geers MGD, Kouznetsova VG. Transient computational homogenization of heterogeneous poroelastic media with local resonances. *Int J Numer Methods Eng*. 2024;e7505. doi: 10.1002/nme.7505

APPENDIX A. FUNDAMENTAL ASSUMPTIONS OF GOVERNING EQUATIONS

Each phase is governed by a different partial differential equation that is derived from the general continuum mechanics balance laws, for example, balance of mass and balance of momentum. The final equations are the result of a linearization procedure combined with appropriate constitutive relations. In fact, as far as the fluid is concerned, the linearization process is based on the small field disturbances around its thermodynamic equilibrium state,^{72, 73} allowing nonlinear

convective terms to be neglected in the absence of mean flow. Equivalently, for the solid phase, the same conclusions are drawn in Reference 8 when considering the small-strain limit. Under these conditions, the material derivative is equivalent to the spatial time derivative. From this point on, the material derivative is used for its conveniently clean notation.

$$\frac{\partial}{\partial t}(\cdot) \equiv (\cdot)'. \quad (\text{A1})$$

Since this work aims to upscale the longwave transient microscopic response, for simplicity, nondissipative constitutive relations for both solid and fluid are considered, so that each phase can be described by a single dependent field variable: the canonical (\vec{u}, p) -formulation used in vibro-acoustic problems.⁵²

Hook's law is the constitutive relation considered for connecting the solid's Cauchy stress with its kinematics, which combined with the linearized balance of linear momentum yields the final governing equation for the solid phase:

$$\left(\rho_s \ddot{\vec{u}} \right) - \vec{\nabla} \cdot \left({}^4\mathbf{C}_s : \vec{\nabla} \vec{u} \right) = \vec{0} \quad \text{in } \Omega_s. \quad (\text{A2})$$

Since sound disturbances are adiabatic,⁷³ the constitutive relation considered connecting stress, that is, pressure disturbance, to its kinematic disturbance is the thermodynamic relation $p = c_0^2 \rho'$ where $c_0 = \sqrt{K_f / \rho_f}$ is the speed of sound in the fluid at quiescent background. Using the previous relation combined with the linearized balance of mass and the linearized balance of linear momentum to eliminate the density disturbance ρ' and the fluid velocity \vec{U} , leads to the final fluid phase wave equation:

$$-\left(-\frac{1}{K_f} \ddot{p} \right) + \vec{\nabla} \cdot \left(-\frac{1}{\rho_f} \vec{\nabla} p \right) = 0 \quad \text{in } \Omega_f. \quad (\text{A3})$$

Finally, the linear set of partial differential Equations (A2) and (A3) govern the aggregate's dynamics, solved via the dependent variables: the solid displacement $\vec{u}(\vec{x}, t)$ and the fluid pressure disturbance $p(\vec{x}, t)$. Equations (A2) and (A3) typically use Lagrangian and Eulerian descriptions, respectively. However, both descriptions may be used interchangeably under the linearized-small-strain limit when there is nearly no difference between current and deformed configurations as well as when external body forces (gravitational force) are neglected.^{52,54} One direct consequence of these assumptions is that the normal to the solid-fluid interface depends only on the position \vec{x} .

APPENDIX B. PROJECTION ON REDUCED SPACE

Nonsymmetric discretized matrix equation

$$\begin{bmatrix} \underline{\lambda}_{BB} & \underline{\lambda}_{BI} \\ \underline{\lambda}_{IB} & \underline{\lambda}_{II} \end{bmatrix} \begin{bmatrix} \underline{\dot{\mathbf{W}}}_B \\ \underline{\dot{\mathbf{W}}}_I \end{bmatrix} + \begin{bmatrix} \underline{\mu}_{BB} & \underline{\mu}_{BI} \\ \underline{\mu}_{IB} & \underline{\mu}_{II} \end{bmatrix} \begin{bmatrix} \underline{\mathbf{W}}_B \\ \underline{\mathbf{W}}_I \end{bmatrix} = \begin{bmatrix} \underline{\mathbf{f}}_B^{\text{ext}} \\ \underline{\mathbf{Q}}_I \end{bmatrix} \quad (\text{B1})$$

\equiv

$$\begin{bmatrix} \left[\begin{array}{cc} \underline{\mathbf{M}}_{bb} & \underline{\mathbf{Q}}_{bb'} \\ \underline{\mathbf{C}}_{b'b} & \underline{\mathbf{Q}}_{b'b'} \end{array} \right] & \left[\begin{array}{cc} \underline{\mathbf{M}}_{bi} & \underline{\mathbf{Q}}_{bi'} \\ \underline{\mathbf{C}}_{b'i} & \underline{\mathbf{Q}}_{b'i'} \end{array} \right] \\ \left[\begin{array}{cc} \underline{\mathbf{M}}_{ib} & \underline{\mathbf{Q}}_{ib'} \\ \underline{\mathbf{C}}_{i'b} & \underline{\mathbf{Q}}_{i'b'} \end{array} \right] & \left[\begin{array}{cc} \underline{\mathbf{M}}_{ii} & \underline{\mathbf{Q}}_{ii'} \\ \underline{\mathbf{C}}_{i'i} & \underline{\mathbf{Q}}_{i'i'} \end{array} \right] \end{bmatrix} \begin{bmatrix} \underline{\ddot{\mathbf{u}}}_b \\ \underline{\ddot{\mathbf{p}}}_{b'} \\ \underline{\ddot{\mathbf{u}}}_i \\ \underline{\ddot{\mathbf{p}}}_{i'} \end{bmatrix} + \begin{bmatrix} \underline{\mathbf{K}}_{bb} & \underline{\mathbf{C}}_{bb'} \\ \underline{\mathbf{Q}}_{b'b} & \underline{\mathbf{H}}_{b'b'} \\ \underline{\mathbf{K}}_{bi} & \underline{\mathbf{C}}_{bi'} \\ \underline{\mathbf{Q}}_{b'i} & \underline{\mathbf{H}}_{b'i'} \end{bmatrix} \begin{bmatrix} \underline{\mathbf{K}}_{bb} & \underline{\mathbf{C}}_{bb'} \\ \underline{\mathbf{Q}}_{b'b} & \underline{\mathbf{H}}_{b'b'} \\ \underline{\mathbf{K}}_{bi} & \underline{\mathbf{C}}_{bi'} \\ \underline{\mathbf{Q}}_{b'i} & \underline{\mathbf{H}}_{b'i'} \end{bmatrix} \begin{bmatrix} \underline{\mathbf{u}}_b \\ \underline{\mathbf{p}}_{b'} \\ \underline{\mathbf{u}}_i \\ \underline{\mathbf{p}}_{i'} \end{bmatrix} = \begin{bmatrix} \underline{\mathbf{f}}_b^{\text{ext}} \\ -\underline{\mathbf{q}}_{b'}^{\text{ext}} \\ \underline{\mathbf{Q}}_i \\ \underline{\mathbf{Q}}_{i'} \end{bmatrix}. \quad (\text{B2})$$

The dynamic behavior described by a system of B + I Equation (30) is reduced to a system of B + Q equations through the projection

$$\begin{bmatrix} \underline{\lambda}_{BB} & \underline{\lambda}_{BI} \\ \underline{\lambda}_{IB} & \underline{\lambda}_{II} \end{bmatrix} \begin{bmatrix} \underline{\dot{\mathbf{W}}}_B \\ \underline{\dot{\mathbf{W}}}_I \end{bmatrix} + \begin{bmatrix} \underline{\mu}_{BB} & \underline{\mu}_{BI} \\ \underline{\mu}_{IB} & \underline{\mu}_{II} \end{bmatrix} \begin{bmatrix} \underline{\mathbf{W}}_B \\ \underline{\mathbf{W}}_I \end{bmatrix} = \begin{bmatrix} \underline{\mathbf{f}}_B^{\text{ext}} \\ \underline{\mathbf{Q}}_I \end{bmatrix} \xrightarrow{\text{proj. reduced basis(42)}} \begin{bmatrix} \underline{\lambda}_{BQ}^{(lr)} & \underline{\lambda}_{QB}^{(c)} \\ \underline{\lambda}_{BQ}^{(c)} & \underline{\lambda}_{BB}^{(lr)} \end{bmatrix} \begin{bmatrix} \underline{\dot{\eta}}_Q \\ \underline{\dot{\mathbf{W}}}_B \end{bmatrix} + \begin{bmatrix} \underline{\Lambda}_{BQ}^{(lr)} & \underline{\mathbf{Q}}_{QB} \\ \underline{\mathbf{Q}}_{BQ} & \underline{\Lambda}_{BB}^{(lr)} \end{bmatrix} \begin{bmatrix} \underline{\eta}_Q \\ \underline{\mathbf{W}}_B \end{bmatrix} = \begin{bmatrix} \underline{\mathbf{Q}}_Q \\ \underline{\mathbf{f}}_B^{\text{ext}} \end{bmatrix}, \quad (\text{B3})$$

where $\underline{I}_{QQ}^{(lr)}$ is an identity matrix and $\underline{\Lambda}_{QQ}^{(lr)}$ is a diagonal matrix of the Q-lowest eigenfrequencies squared related to the time-harmonic BVP (33). The matrices $\underline{\lambda}_{BB}^{(lw)}$, $\underline{\mu}_{BB}^{(lw)}$ are, respectively, the generalized mass and stiffness matrices related to the steady-state BVP (32). The terms $\underline{\lambda}_{QB}^{(c)}$ and $\underline{\lambda}_{BQ}^{(c)}$ are the coupling between the longwave space and local resonance space, see Appendix B the projection that leads to

$$\begin{aligned}\underline{I}_{QQ}^{(lr)} &= \underline{\Psi}_{IQ}^T \underline{\lambda}_{II} \underline{\Phi}_{IQ} \\ \underline{\Lambda}_{QQ}^{(lr)} &= \underline{\Psi}_{IQ}^T \underline{\mu}_{II} \underline{\Phi}_{IQ} \\ \underline{\lambda}_{BB}^{(lw)} &= \underline{\lambda}_{BB} + \underline{\lambda}_{BI} \underline{S}_{IB} + \underline{Y}_{IB}^T \underline{\lambda}_{IB} + \underline{Y}_{IB}^T \underline{\lambda}_{II} \underline{S}_{IB} \\ \underline{\mu}_{BB}^{(lw)} &= \underline{\mu}_{BB} + \underline{\mu}_{BI} \underline{S}_{IB} + \underline{Y}_{IB}^T \underline{\mu}_{IB} + \underline{Y}_{IB}^T \underline{\mu}_{II} \underline{S}_{IB} \\ \underline{\lambda}_{QB}^{(c)} &= \underline{\Psi}_{IQ}^T \underline{\lambda}_{IB} + \underline{\Psi}_{IQ}^T \underline{\lambda}_{II} \underline{S}_{IB} \\ \underline{\lambda}_{BQ}^{(c)} &= \underline{\lambda}_{BI} \underline{\Phi}_{IQ} + \underline{Y}_{IB}^T \underline{\lambda}_{II} \underline{\Phi}_{IQ},\end{aligned}\quad (B4)$$

where the matrices \underline{Y}_{IB}^T and \underline{S}_{IB} are the left- and right-longwave modes, the $\underline{\Psi}_{IQ}^T$ and $\underline{\Phi}_{IQ}$ are the left- and right-eigenmodes normalized with respect to the mass submatrix $\underline{\lambda}_{II}$, and here, the index is shown to indicate the consistency between matrix multiplications. The expansion of the longwave generalized stiffness matrix read as

$$\begin{aligned}\underline{\mu}_{BB}^{(lw)} &= \underline{\mu}_{BB} + \underline{\mu}_{BI} \underline{S}_{IB} + \underline{Y}_{IB}^T \underline{\mu}_{IB} + \underline{Y}_{IB}^T \underline{\mu}_{II} \underline{S}_{IB} \\ &= \underline{\mu}_{BB} + \underline{\mu}_{BI} \left(-\underline{\mu}_{II}^{-1} \underline{\mu}_{IB} \right) + \left(-\underline{\mu}_{BI} \underline{\mu}_{II}^{-1} \right) \underline{\mu}_{IB} + \left(-\underline{\mu}_{BI} \underline{\mu}_{II}^{-1} \right) \underline{\mu}_{II} \left(-\underline{\mu}_{II}^{-1} \underline{\mu}_{IB} \right) \\ &= \underline{\mu}_{BB} - \underline{\mu}_{BI} \underline{\mu}_{II}^{-1} \underline{\mu}_{IB} - \underline{\mu}_{BI} \underline{\mu}_{II}^{-1} \underline{\mu}_{IB} + \underline{\mu}_{BI} \underline{\mu}_{II}^{-1} \underline{\mu}_{II} \underline{\mu}_{II}^{-1} \underline{\mu}_{IB} \\ &= \underline{\mu}_{BB} - \underline{\mu}_{BI} \underline{\mu}_{II}^{-1} \underline{\mu}_{IB} \\ &= \begin{bmatrix} \underline{\mathbf{K}}_{bb} & \underline{\vec{C}}_{bb'} \\ \underline{\vec{0}}_{b'b} & \underline{H}_{b'b'} \end{bmatrix} - \begin{bmatrix} \underline{\mathbf{K}}_{bi} & \underline{\vec{C}}_{bi'} \\ \underline{\vec{0}}_{b'i} & \underline{H}_{b'i'} \end{bmatrix} \begin{bmatrix} \underline{\mathbf{K}}_{ii} & \underline{\vec{C}}_{ii'} \\ \underline{\vec{0}}_{i'i} & \underline{H}_{i'i'} \end{bmatrix}^{-1} \begin{bmatrix} \underline{\mathbf{K}}_{ib} & \underline{\vec{C}}_{ib'} \\ \underline{\vec{0}}_{i'b} & \underline{H}_{i'b'} \end{bmatrix} \\ &= \begin{bmatrix} \underline{\mathbf{K}}_{bb} & \underline{\vec{C}}_{bb'} \\ \underline{\vec{0}}_{b'b} & \underline{H}_{b'b'} \end{bmatrix} - \begin{bmatrix} \underline{\mathbf{K}}_{bi} & \underline{\vec{C}}_{bi'} \\ \underline{\vec{0}}_{b'i} & \underline{H}_{b'i'} \end{bmatrix} \begin{bmatrix} \underline{\mathbf{K}}_{ii}^{-1} & -\underline{\mathbf{K}}_{ii}^{-1} \underline{\vec{C}}_{ii'} \underline{H}_{i'i'}^{-1} \\ \underline{\vec{0}}_{i'i} & \underline{H}_{i'i'}^{-1} \end{bmatrix} \begin{bmatrix} \underline{\mathbf{K}}_{ib} & \underline{\vec{C}}_{ib'} \\ \underline{\vec{0}}_{i'b} & \underline{H}_{i'b'} \end{bmatrix} \\ &\equiv \begin{bmatrix} \underline{\mu}_{bb} & \underline{\vec{\mu}}_{bb'} \\ \underline{\vec{0}}_{b'b} & \underline{\mu}_{b'b'} \end{bmatrix}\end{aligned}\quad (B5)$$

and the longwave generalized mass matrix as

$$\begin{aligned}\underline{\lambda}_{BB}^{(lw)} &= \underline{\lambda}_{BB} + \underline{\lambda}_{BI} \underline{S}_{IB} + \underline{Y}_{IB}^T \underline{\lambda}_{IB} + \underline{Y}_{IB}^T \underline{\lambda}_{II} \underline{S}_{IB} \\ &= \begin{bmatrix} \underline{\mathbf{M}}_{bb} & \underline{\vec{0}}_{bb'} \\ \underline{\vec{C}}_{b'b} & \underline{Q}_{b'b'} \end{bmatrix} + \begin{bmatrix} \underline{\mathbf{M}}_{bi} & \underline{\vec{0}}_{bi'} \\ \underline{\vec{C}}_{b'i} & \underline{Q}_{i'i'} \end{bmatrix} \begin{bmatrix} \underline{\Sigma}_{ib} & \underline{\vec{\Sigma}}_{ib'} \\ \underline{\vec{0}}_{i'b} & \underline{\Sigma}_{i'b'} \end{bmatrix} + \begin{bmatrix} \underline{\mathbf{Y}}_{bi} & \underline{\vec{Y}}_{bi'} \\ \underline{\vec{0}}_{b'i} & \underline{Y}_{b'i'} \end{bmatrix} \begin{bmatrix} \underline{\mathbf{M}}_{ib} & \underline{\vec{0}}_{ib'} \\ \underline{\vec{C}}_{i'b} & \underline{Q}_{i'b'} \end{bmatrix} \\ &\quad + \begin{bmatrix} \underline{\mathbf{Y}}_{bi} & \underline{\vec{Y}}_{bi'} \\ \underline{\vec{0}}_{b'i} & \underline{Y}_{b'i'} \end{bmatrix} \begin{bmatrix} \underline{\mathbf{M}}_{ii} & \underline{\vec{0}}_{ii'} \\ \underline{\vec{C}}_{i'i} & \underline{Q}_{i'i'} \end{bmatrix} \begin{bmatrix} \underline{\Sigma}_{ib} & \underline{\vec{\Sigma}}_{ib'} \\ \underline{\vec{0}}_{i'b} & \underline{\Sigma}_{i'b'} \end{bmatrix} \\ &\equiv \begin{bmatrix} \underline{\lambda}_{bb} & \underline{\vec{\lambda}}_{bb'} \\ \underline{\vec{\lambda}}_{b'b} & \underline{\lambda}_{b'b'} \end{bmatrix}.\end{aligned}\quad (B6)$$

APPENDIX C. EVOLUTION EQUATIONS AND MACROSCOPIC CONSTITUTIVE RELATIONS

The reduced set of Equations (44),(43) in terms of $\underline{\mathbb{W}}_B$ is rewritten in the $[\underline{\vec{u}}_b \ \underline{p}_{b'}]^T$ format, separating the fluid and solid parts leading to

$$\mathbf{I}_{\text{QQ}}^{(\text{lr})} \ddot{\eta}_{\text{Q}} + \mathbf{\Lambda}_{\text{QQ}}^{(\text{lr})} \eta_{\text{Q}} = - \overbrace{\left[\begin{array}{cc} \underline{\vec{m}}_{\text{Qb}} & \underline{\vec{m}}_{\text{Qb}'} \end{array} \right]}^{\mathbf{\Lambda}_{\text{QB}}^{(\text{c})} \equiv} \underbrace{\left[\begin{array}{c} \ddot{\vec{u}}_{\text{b}} \\ \ddot{\vec{p}}_{\text{b}'} \end{array} \right]}_{= \ddot{\vec{\Psi}}_{\text{B}}, \text{ Equation (31)}} \quad (\text{C1})$$

and

$$\overbrace{\left[\begin{array}{cc} \underline{\lambda}_{\text{bb}} & \underline{\vec{\lambda}}_{\text{bb}'} \\ \underline{\vec{\lambda}}_{\text{b'b}} & \underline{\lambda}_{\text{b'b}'} \end{array} \right]}^{\mathbf{\Lambda}_{\text{BB}}^{(\text{lw})} \equiv} \left[\begin{array}{c} \ddot{\vec{u}}_{\text{b}} \\ \ddot{\vec{p}}_{\text{b}'} \end{array} \right] + \overbrace{\left[\begin{array}{cc} \underline{\mu}_{\text{bb}} & \underline{\vec{\mu}}_{\text{bb}'} \\ \underline{\vec{0}}_{\text{b'b}} & \underline{\mu}_{\text{b'b}'} \end{array} \right]}^{\mathbf{\Lambda}_{\text{BB}}^{(\text{lw})} \equiv} \left[\begin{array}{c} \ddot{\vec{u}}_{\text{b}} \\ \ddot{\vec{p}}_{\text{b}'} \end{array} \right] + \overbrace{\left[\begin{array}{c} \underline{\vec{m}}_{\text{bQ}} \\ \underline{\vec{m}}_{\text{b'Q}} \end{array} \right]}^{\mathbf{\Lambda}_{\text{BQ}}^{(\text{c})} \equiv} \ddot{\eta}_{\text{Q}} = \underbrace{\left[\begin{array}{c} \vec{f}_{\text{b}}^{\text{ext}} \\ -\vec{q}_{\text{b}'}^{\text{ext}} \end{array} \right]}_{= \vec{f}_{\text{B}}^{\text{ext}}, \text{ Equation (31)}} \quad (\text{C2})$$

The matrix expressions in terms of the original discretized system (28) are given by Equation (B4). Note that $\mathbf{\Lambda}_{\text{BB}}^{(\text{lw})}$ has an identically zero submatrix matrix $\vec{0}_{\text{b'b}}$ meaning that external fluid flux is insensitive to the quasistatic solid displacements. Later on, the macroscopic constitutive relations of the fluid volumetric strain and acceleration, as a consequence, will not depend to the solid displacement and its gradient. Inserting Equation (46) in Equation (C1), we have

$$\begin{aligned} \mathbf{I}_{\text{QQ}}^{(\text{lr})} \ddot{\eta}_{\text{Q}} + \mathbf{\Lambda}_{\text{QQ}}^{(\text{lr})} \eta_{\text{Q}} &= -\mathbf{\Lambda}_{\text{QB}}^{(\text{c})} \ddot{\vec{\Psi}}_{\text{B}} \\ &= - \left[\begin{array}{cc} \underline{\vec{m}}_{\text{Qb}} & \underline{\vec{m}}_{\text{Qb}'} \end{array} \right] \left[\begin{array}{c} \ddot{\vec{u}}_{\text{b}} \\ \ddot{\vec{p}}_{\text{b}'} \end{array} \right] \\ &= -\underline{\vec{m}}_{\text{Qb}} \cdot \left(\underline{\mathbf{1}}_{\text{b}} \ddot{\vec{u}}_{\text{M}} + \left(\vec{\nabla}_{\text{M}} \ddot{\vec{u}}_{\text{M}} \right)^{\text{T}} \cdot \Delta \vec{\tilde{x}}_{\text{b}} \right) \\ &= -\underline{\vec{m}}_{\text{Qb}} \cdot \left(\underline{\mathbf{1}}_{\text{b}} \ddot{\vec{u}}_{\text{M}} + \left(\vec{\nabla}_{\text{M}} \ddot{\vec{u}}_{\text{M}} \right)^{\text{T}} \cdot \Delta \vec{\tilde{x}}_{\text{b}} \right) \\ &\quad - \underline{\vec{m}}_{\text{Qb}'} \cdot \left(\underline{\mathbf{1}}_{\text{b}'} \ddot{p}_{\text{M}} + \vec{\nabla}_{\text{M}} \ddot{p}_{\text{M}} \cdot \Delta \vec{\tilde{x}}_{\text{b}'} \right) \\ &= - \left[\underline{\vec{m}}_{\text{Qb}} \underline{\mathbf{1}}_{\text{b}} \right] \cdot \ddot{\vec{u}}_{\text{M}} - \left[\underline{\vec{m}}_{\text{Qb}} \otimes \Delta \vec{\tilde{x}}_{\text{b}} \right] : \vec{\nabla}_{\text{M}} \ddot{\vec{u}}_{\text{M}} \\ &\quad - \left[\underline{\vec{m}}_{\text{Qb}'} \underline{\mathbf{1}}_{\text{b}'} \right] \ddot{p}_{\text{M}} - \left[\underline{\vec{m}}_{\text{Qb}'} \Delta \vec{\tilde{x}}_{\text{b}'} \right] \cdot \vec{\nabla}_{\text{M}} \ddot{p}_{\text{M}} \end{aligned} \quad (\text{C3})$$

The matrix equation above is rewritten for each mode j separately since the left-hand side matrices are diagonal and the right-hand side are vectors, leading to the evolution Equation (48):

$$\ddot{\eta}_j + \omega_j^2 \eta_j = - \vec{\alpha}_j \cdot \ddot{\vec{u}}_{\text{M}} - \beta_j : \vec{\nabla}_{\text{M}} \ddot{\vec{u}}_{\text{M}} + \gamma_j \ddot{p}_{\text{M}} + \vec{\delta}_j \cdot \vec{\nabla}_{\text{M}} \ddot{p}_{\text{M}} \quad \text{for eigenmodes} \quad j = 1, 2, \dots, Q. \quad (\text{C4})$$

The reduced set of Equation (44) is used for computing the external micro fluxes $\vec{f}_{\text{b}}^{\text{ext}}$ and $\vec{q}_{\text{b}'}^{\text{ext}}$ that can be found by inserting Equation (46) in Equation (44). After this step, they are inserted in the discretized Equation (45), providing closed-form constitutive relations for the macroscopic solid momentum

$$\begin{aligned}
(1 - \phi) \dot{\tilde{\pi}}_M &= \frac{1}{V} \begin{bmatrix} \mathbf{1}_b^T & \underline{\lambda}_{bb} & \mathbf{1}_b \end{bmatrix}_{\text{Biot}} \cdot \ddot{\mathbf{u}}_M + \frac{1}{V} \begin{bmatrix} \mathbf{1}_b^T & \underline{\lambda}_{bb} & \otimes \Delta \tilde{\mathbf{x}}_b \end{bmatrix} : \vec{\nabla} \ddot{\mathbf{u}}_M \\
&+ \frac{1}{V} \begin{bmatrix} \mathbf{1}_b^T & \underline{\lambda}_{bb'} & \mathbf{1}_b \end{bmatrix} \ddot{\mathbf{p}}_M + \frac{1}{V} \begin{bmatrix} \mathbf{1}_b^T & \underline{\lambda}_{bb'} & \otimes \Delta \tilde{\mathbf{x}}_{b'} \end{bmatrix} \cdot \vec{\nabla} \ddot{\mathbf{p}}_M \\
&+ \frac{1}{V} \begin{bmatrix} \mathbf{1}_b^T & \underline{\mu}_{bb} & \mathbf{1}_b \end{bmatrix} \cdot \ddot{\mathbf{u}}_M + \frac{1}{V} \begin{bmatrix} \mathbf{1}_b^T & \underline{\mu}_{bb} & \otimes \Delta \tilde{\mathbf{x}}_b \end{bmatrix} : \vec{\nabla} \ddot{\mathbf{u}}_M \\
&+ \frac{1}{V} \begin{bmatrix} \mathbf{1}_b^T & \underline{\mu}_{bb'} & \mathbf{1}_b \end{bmatrix} \ddot{\mathbf{p}}_M + \frac{1}{V} \begin{bmatrix} \mathbf{1}_b^T & \underline{\mu}_{bb'} & \otimes \Delta \tilde{\mathbf{x}}_{b'} \end{bmatrix}_{\text{Biot}} \cdot \vec{\nabla} \ddot{\mathbf{p}}_M \\
&+ \frac{1}{V} \begin{bmatrix} \mathbf{1}_b^T & \underline{\mathbf{m}}_{bQ} \end{bmatrix}^T \ddot{\eta}_Q
\end{aligned} \tag{C5}$$

for the macroscopic solid stress

$$\begin{aligned}
(1 - \phi) \sigma_M &= \frac{1}{V} \left[\Delta \tilde{\mathbf{x}}_b^T \otimes \underline{\lambda}_{bb} \mathbf{1}_b \right]^{\text{LT}} \cdot \ddot{\mathbf{u}}_M + \frac{1}{V} \left[\Delta \tilde{\mathbf{x}}_b^T \otimes \underline{\lambda}_{bb} \otimes \Delta \tilde{\mathbf{x}}_b \right]^{\text{LT}} : \vec{\nabla} \ddot{\mathbf{u}}_M \\
&+ \frac{1}{V} \left[\Delta \tilde{\mathbf{x}}_b^T \otimes \underline{\lambda}_{bb'} \mathbf{1}_{b'} \right] \ddot{\mathbf{p}}_M + \frac{1}{V} \left[\Delta \tilde{\mathbf{x}}_b^T \otimes \underline{\lambda}_{bb'} \otimes \Delta \tilde{\mathbf{x}}_{b'} \right] \cdot \vec{\nabla} \ddot{\mathbf{p}}_M \\
&+ \frac{1}{V} \left[\Delta \tilde{\mathbf{x}}_b^T \otimes \underline{\mu}_{bb} \mathbf{1}_b \right]^{\text{LT}} \cdot \ddot{\mathbf{u}}_M + \frac{1}{V} \left[\Delta \tilde{\mathbf{x}}_b^T \otimes \underline{\mu}_{bb} \otimes \Delta \tilde{\mathbf{x}}_b \right]^{\text{LT}}_{\text{Biot}} : \vec{\nabla} \ddot{\mathbf{u}}_M \\
&+ \frac{1}{V} \left[\Delta \tilde{\mathbf{x}}_b^T \otimes \underline{\mu}_{bb'} \mathbf{1}_{b'} \right]_{\text{Biot}} \ddot{\mathbf{p}}_M + \frac{1}{V} \left[\Delta \tilde{\mathbf{x}}_b^T \otimes \underline{\mu}_{bb'} \otimes \Delta \tilde{\mathbf{x}}_{b'} \right] \cdot \vec{\nabla} \ddot{\mathbf{p}}_M \\
&+ \frac{1}{V} \left[\underline{\mathbf{m}}_{bQ}^T \otimes \Delta \tilde{\mathbf{x}}_b \right]^T \ddot{\eta}_Q
\end{aligned} \tag{C6}$$

for the fluid volumetric strain rate

$$\begin{aligned}
\phi \dot{\tilde{\epsilon}}_M &= -\frac{1}{V} \begin{bmatrix} \mathbf{1}_{b'}^T & \underline{\lambda}_{b'b} & \mathbf{1}_b \end{bmatrix} \cdot \ddot{\mathbf{u}}_M - \frac{1}{V} \begin{bmatrix} \mathbf{1}_{b'}^T & \underline{\lambda}_{b'b} & \otimes \Delta \tilde{\mathbf{x}}_b \end{bmatrix}_{\text{Biot}} : \vec{\nabla} \ddot{\mathbf{u}}_M \\
&- \frac{1}{V} \begin{bmatrix} \mathbf{1}_{b'}^T & \underline{\lambda}_{b'b'} & \mathbf{1}_{b'} \end{bmatrix}_{\text{Biot}} \ddot{\mathbf{p}}_M - \frac{1}{V} \begin{bmatrix} \mathbf{1}_{b'}^T & \underline{\lambda}_{b'b'} & \otimes \Delta \tilde{\mathbf{x}}_{b'} \end{bmatrix} \cdot \vec{\nabla} \ddot{\mathbf{p}}_M \\
&- \frac{1}{V} \begin{bmatrix} \mathbf{1}_{b'}^T & \underline{\mu}_{b'b} & \mathbf{1}_b \end{bmatrix} \cdot \ddot{\mathbf{u}}_M - \frac{1}{V} \begin{bmatrix} \mathbf{1}_{b'}^T & \underline{\mu}_{b'b} & \otimes \Delta \tilde{\mathbf{x}}_b \end{bmatrix} : \vec{\nabla} \ddot{\mathbf{u}}_M \\
&- \frac{1}{V} \begin{bmatrix} \mathbf{1}_{b'}^T & \underline{\mu}_{b'b'} & \mathbf{1}_{b'} \end{bmatrix} \ddot{\mathbf{p}}_M - \frac{1}{V} \begin{bmatrix} \mathbf{1}_{b'}^T & \underline{\mu}_{b'b'} & \otimes \Delta \tilde{\mathbf{x}}_{b'} \end{bmatrix} \cdot \vec{\nabla} \ddot{\mathbf{p}}_M \\
&- \frac{1}{V} \begin{bmatrix} \mathbf{1}_{b'}^T & \underline{\mathbf{m}}_{b'Q} \end{bmatrix}^T \ddot{\eta}_Q,
\end{aligned} \tag{C7}$$

and for the fluid acceleration

$$\begin{aligned}
\phi \ddot{\mathbf{U}}_M &= -\frac{1}{V} \left[\Delta \tilde{\mathbf{x}}_{b'}^T \otimes \underline{\lambda}_{b'b} \mathbf{1}_b \right]_{\text{Biot}} \cdot \ddot{\mathbf{u}}_M - \frac{1}{V} \left[\Delta \tilde{\mathbf{x}}_{b'}^T \otimes \underline{\lambda}_{b'b} \otimes \Delta \tilde{\mathbf{x}}_b \right] : \vec{\nabla} \ddot{\mathbf{u}}_M \\
&- \frac{1}{V} \left[\Delta \tilde{\mathbf{x}}_{b'}^T \otimes \underline{\lambda}_{b'b'} \mathbf{1}_{b'} \right] \ddot{\mathbf{p}}_M - \frac{1}{V} \left[\Delta \tilde{\mathbf{x}}_{b'}^T \otimes \underline{\lambda}_{b'b'} \otimes \Delta \tilde{\mathbf{x}}_{b'} \right] \cdot \vec{\nabla} \ddot{\mathbf{p}}_M \\
&- \frac{1}{V} \left[\Delta \tilde{\mathbf{x}}_{b'}^T \otimes \underline{\mu}_{b'b} \mathbf{1}_b \right] \cdot \ddot{\mathbf{u}}_M - \frac{1}{V} \left[\Delta \tilde{\mathbf{x}}_{b'}^T \otimes \underline{\mu}_{b'b} \otimes \Delta \tilde{\mathbf{x}}_b \right] : \vec{\nabla} \ddot{\mathbf{u}}_M \\
&- \frac{1}{V} \left[\Delta \tilde{\mathbf{x}}_{b'}^T \otimes \underline{\mu}_{b'b'} \mathbf{1}_{b'} \right] \ddot{\mathbf{p}}_M - \frac{1}{V} \left[\Delta \tilde{\mathbf{x}}_{b'}^T \otimes \underline{\mu}_{b'b'} \otimes \Delta \tilde{\mathbf{x}}_{b'} \right]_{\text{Biot}} \cdot \vec{\nabla} \ddot{\mathbf{p}}_M \\
&- \frac{1}{V} \left[\underline{\mathbf{m}}_{b'Q}^T \otimes \Delta \tilde{\mathbf{x}}_{b'} \right]^T \ddot{\eta}_Q.
\end{aligned} \tag{C8}$$

Or, in short, as Equation (47).

$$\begin{aligned}
(1 - \phi) \dot{\tilde{\pi}}_M &= \mathbf{A}_\pi \cdot \ddot{\mathbf{u}}_M + {}^3\mathbf{B}_\pi : \vec{\nabla} \ddot{\mathbf{u}}_M + \vec{\mathbf{C}}_\pi \ddot{\mathbf{p}}_M + \mathbf{D}_\pi \cdot \vec{\nabla} \ddot{\mathbf{p}}_M \\
&+ \mathbf{E}_\pi \cdot \ddot{\mathbf{u}}_M + {}^3\mathbf{F}_\pi : \vec{\nabla} \ddot{\mathbf{u}}_M + \vec{\mathbf{G}}_\pi \ddot{\mathbf{p}}_M + \mathbf{H}_\pi \cdot \vec{\nabla} \ddot{\mathbf{p}}_M + \sum_{j=1}^Q \vec{\mathbf{a}}_j \ddot{\eta}_j, \\
(1 - \phi) \sigma_M &= {}^3\mathbf{A}_\sigma \cdot \ddot{\mathbf{u}}_M + {}^4\mathbf{B}_\sigma : \vec{\nabla} \ddot{\mathbf{u}}_M + \mathbf{C}_\sigma \ddot{\mathbf{p}}_M + {}^3\mathbf{D}_\sigma \cdot \vec{\nabla} \ddot{\mathbf{p}}_M \\
&+ {}^3\mathbf{E}_\sigma \cdot \ddot{\mathbf{u}}_M + {}^4\mathbf{F}_\sigma : \vec{\nabla} \ddot{\mathbf{u}}_M + \mathbf{G}_\sigma \ddot{\mathbf{p}}_M + {}^3\mathbf{H}_\sigma \cdot \vec{\nabla} \ddot{\mathbf{p}}_M + \sum_{j=1}^Q \mathbf{b}_j \ddot{\eta}_j,
\end{aligned}$$

$$\begin{aligned}
\phi \ddot{\mathbf{u}}_M &= \vec{A}_\epsilon \cdot \ddot{\mathbf{u}}_M + \mathbf{B}_\epsilon : \vec{\nabla} \ddot{\mathbf{u}}_M + C_\epsilon \ddot{\mathbf{p}}_M + \vec{D}_\epsilon \cdot \vec{\nabla} \ddot{\mathbf{p}}_M \\
&+ \vec{E}_\epsilon \cdot \ddot{\mathbf{u}}_M + \mathbf{F}_\epsilon : \vec{\nabla} \ddot{\mathbf{u}}_M + G_\epsilon \ddot{\mathbf{p}}_M + \vec{H}_\epsilon \cdot \vec{\nabla} \ddot{\mathbf{p}}_M + \sum_{j=1}^Q c_j \ddot{\eta}_j, \\
\phi \ddot{\mathbf{U}}_M &= \mathbf{A}_U \cdot \ddot{\mathbf{u}}_M + {}^3\mathbf{B}_U : \vec{\nabla} \ddot{\mathbf{u}}_M + \vec{C}_U \ddot{\mathbf{p}}_M + \mathbf{D}_U \cdot \vec{\nabla} \ddot{\mathbf{p}}_M \\
&+ \mathbf{E}_U \cdot \ddot{\mathbf{u}}_M + {}^3\mathbf{F}_U : \vec{\nabla} \ddot{\mathbf{u}}_M + \vec{G}_U \ddot{\mathbf{p}}_M + \mathbf{H}_U \cdot \vec{\nabla} \ddot{\mathbf{p}}_M + \sum_{j=1}^Q \vec{d}_j \ddot{\eta}_j.
\end{aligned}$$

It is shown in Appendix B, that the longwave generalized stiffness matrix $\underline{\mathbb{J}}_{\text{BB}}^{(\text{lw})}$ is the product of upper triangular matrices, hence, it also assumes the upper triangular form

$$\underline{\mathbb{J}}_{\text{BB}}^{(\text{lw})} \equiv \begin{bmatrix} \underline{\mu}_{bb} & \underline{\mu}_{bb'} \\ \underline{0}_{b'b} & \underline{\mu}_{b'b'} \end{bmatrix}. \quad (\text{C9})$$

Since the coefficients \vec{E}_ϵ , \mathbf{F}_ϵ , \mathbf{E}_U , ${}^3\mathbf{F}_U$ depend on the lower off-diagonal submatrix $\underline{\mu}_{b'b} = \vec{0}_{b'b}$, they vanish identically by construction. The coefficients \mathbf{E}_π , ${}^3\mathbf{F}_\pi$ and ${}^3\mathbf{E}_\sigma$ depend on the product $\underline{\mu}_{bb} \underline{1}_b$, vanishing identically, since $\underline{1}_b$ belongs to the null-space of $\underline{\mu}_{bb}$, describing the rigid body mode of the prescribed nodes b . Analogously, the coefficients G_ϵ , \vec{H}_ϵ and \vec{G}_U depend on the product $\underline{\mu}_{b'b'} \underline{1}_{b'}$, vanishing identically, since $\underline{1}_{b'}$ belongs to the null-space of $\underline{\mu}_{b'b'}$. The mathematically analogous to the solid rigid body motion is the fluid phase under a homogeneous increase in pressure $\underline{1}_{b'}$ to the prescribed nodes b' , in the absence of flow, in other words, a homogeneous volume expansion/contraction takes place under these circumstances. Thus, the eigenvalue problem neglecting the identically zero coefficients reads

$$\begin{aligned}
(-\omega^2) \begin{bmatrix} \mathbf{A}_\pi + \vec{k} \cdot {}^4\mathbf{B}_\sigma^{\text{LT}} \cdot \vec{k} + i(-{}^3\mathbf{B}_\pi \cdot \vec{k} + \vec{k} \cdot {}^3\mathbf{A}_\sigma^{\text{LT}}) & \vec{C}_\pi + \vec{k} \cdot {}^3\mathbf{D}_\sigma^{\text{LT}} \cdot \vec{k} + i(-\mathbf{D}_\pi \cdot \vec{k} + \vec{k} \cdot \mathbf{C}_\sigma^{\text{T}}) & (\vec{a} + i\vec{k} \cdot \underline{\mathbf{b}})^{\text{T}} \\ \vec{A}_\epsilon + \vec{k} \cdot {}^3\mathbf{B}_U \cdot \vec{k} + i(-\mathbf{B}_\epsilon \cdot \vec{k} + \vec{k} \cdot \mathbf{A}_U) & C_\epsilon + \vec{k} \cdot \mathbf{D}_U \cdot \vec{k} + i(-\vec{D}_\epsilon \cdot \vec{k} + \vec{k} \cdot \vec{C}_U) & (\vec{c} + i\vec{k} \cdot \underline{\vec{d}})^{\text{T}} \\ \vec{a} + i\vec{k} \cdot (-\underline{\beta}) & -\underline{\gamma} + i\vec{k} \cdot \underline{\vec{d}} & \underline{\mathbb{I}}_{\text{QQ}}^{(\text{lr})} \end{bmatrix} \begin{pmatrix} \hat{\mathbf{u}}_M \\ \hat{\mathbf{p}}_M \\ \hat{\eta}_Q \end{pmatrix} \\
+ \begin{bmatrix} \vec{k} \cdot {}^4\mathbf{F}_\sigma^{\text{LT}} \cdot \vec{k} & \vec{G}_\pi + \vec{k} \cdot {}^3\mathbf{H}_\sigma^{\text{LT}} \cdot \vec{k} + i(-\mathbf{H}_\pi \cdot \vec{k} + \vec{k} \cdot \mathbf{G}_\sigma^{\text{T}}) & \underline{0}_{\text{Q}}^{\text{T}} \\ \vec{0} & \vec{k} \cdot \mathbf{H}_U \cdot \vec{k} & \underline{0}_{\text{Q}}^{\text{T}} \\ \underline{0}_{\text{Q}} & \underline{0}_{\text{Q}} & \underline{\Lambda}_{\text{QQ}}^{(\text{lr})} \end{bmatrix} \begin{pmatrix} \hat{\mathbf{u}}_M \\ \hat{\mathbf{p}}_M \\ \hat{\eta}_Q \end{pmatrix} = \begin{pmatrix} \vec{0} \\ 0 \\ 0 \end{pmatrix}. \quad (\text{C10})
\end{aligned}$$

The motivation for the choice of \vec{x}_R is twofold: it is made such that certain coefficients are significantly reduced (${}^4\mathbf{B}_\sigma$, \mathbf{D}_U) and (${}^3\mathbf{B}_\pi$, ${}^3\mathbf{A}_\sigma$, \vec{D}_ϵ , \vec{C}_U), in which the latter group becomes zero in the case of a square symmetric unit cell such as Liu et al.⁶⁴; and more importantly preserving the symmetries of the operator on the state vector $[\hat{\mathbf{u}}_M \ \hat{\mathbf{p}}_M \ \hat{\eta}_Q]^{\text{T}}$ that leads to an eigenproblem with real eigenvalues, which is expected for a conservative system. It is logical that the eigenvalue problem of the homogenized continuum has real eigenfrequencies since the full-field response does not decay with time, which aligns with the results of Willis⁷⁴ showing that self-adjointness at the microscale implies self-adjointness at the macroscale.

For the considered numerical example of Section 4, placing $\vec{x}_R = \vec{0}$ at the RVE centroid leads to eigenfrequencies with negligible imaginary parts. Moreover, the generalized mass matrix

$$\underline{\mathbb{M}}_{\text{BB}}^{(\text{lw})} \equiv \begin{bmatrix} \underline{\lambda}_{bb} & \underline{\lambda}_{bb'} \\ \underline{\lambda}_{b'b} & \underline{\lambda}_{b'b'} \end{bmatrix} \quad (\text{C11})$$

assumes a quasi-lower triangular form $\underline{\lambda}_{bb'} \approx \vec{0}_{bb'}$, causing the coefficients (\vec{C}_π , \mathbf{D}_π , \mathbf{C}_σ , ${}^3\mathbf{D}_\sigma$) to become approximately zero. The remaining non-Biot coefficients (\vec{G}_π , ${}^3\mathbf{H}_\sigma$, \mathbf{A}_ϵ , \mathbf{B}_U) are non-standard coupling terms between solid and fluid phases that are also approximately zero. The last consideration for the selected numerical example

in this article is that the so-called elastic inertia terms (${}^4\mathbf{B}_\sigma$, \mathbf{D}_U) are also approximately zero. Regarding the local resonance coefficients, since only dipolar modes occur in the solid phase, the coefficients $\mathbf{b}, \mathbf{c}, \mathbf{d}, \mathbf{\beta}, \mathbf{\gamma}, \mathbf{\delta}$ are approximately zero.

APPENDIX D. EFFECTIVE CONSTITUTIVE RESPONSE

First, the dispersion problem (C1) will be considered neglecting the contribution of the local resonances, that is, disregarding the Q mode contributions, the eigenvalue problem reduces to the $[\hat{\mathbf{u}}_M \ \hat{\mathbf{p}}_M]^T$ block having a dimension equal to 3, that is, two displacement components and one pressure component (2D). Hence, three non-degenerated eigenfrequencies are computed.

In Figure D1A, the homogenized continua have three non-dispersive branches that characterize three propagating waves. The branches calculated with the 32 coefficients of the longwave regime—including A_ξ to H_ξ , alphabetically, with index $\xi = \{\pi, \sigma, \epsilon, U\}$ are plotted as solid red lines (—) whereas the branches calculated with only the Biot coefficients (51) are plotted in dashed blue lines (---). The branches remain practically the same, leading to an effective constitutive behavior equivalent to the one predicted by Biot theory, numerically demonstrating the effective Biot continuum behavior pointed out in Section 3.4.

In Figure D1A the $\omega(\vec{k})$ -curves are shown up to frequencies of $f_{\max} \approx 1600$ Hz which correspond, for the lowest branch, to a wavevector of $\vec{k} = \pi/(4a_x)\vec{e}_x$, that is, for the lowest branch the shortest propagating wavelength is approximately one order of magnitude greater than the unit cell size ($\lambda = 2\pi/||\vec{k}|| = 8a_x$) fulfilling to the separation of scales condition established in Section 2.3. Hence, it approximately defines the upper-bound frequency f_{\max} for the validity of the longwave homogenization. It originates purely from geometrical arguments considering $l^{(\text{host})} = a_x$ as the characteristic length of the *host* medium, yielding the frequency range of $[f_{\min}, f_{\max}] = [20, 1600]$ Hz.

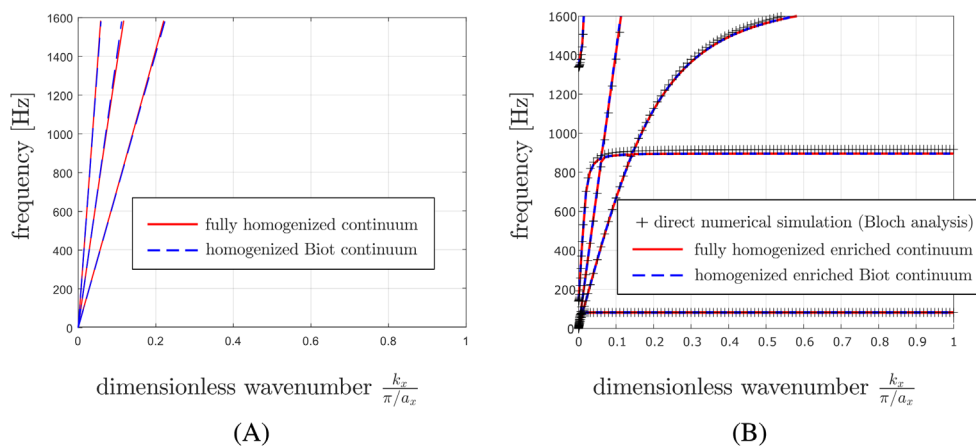


FIGURE D1 (A) Three non-dispersive curves are computed neglecting the resonant mode contributions. The red lines (—) show the branches of the fully homogenized continuum and the dashed blue lines (---) show the branches of the homogenized Biot continuum. (B) The dispersion curve of DNS (+), fully homogenized enriched continuum in red lines (—), and homogenized enriched Biot continuum in dashed blue lines (---). Table D1 specifies the constitutive model used for each case.

TABLE D1 Coefficients included in each constitutive model.

Continuum type	Longwave coefficients	Local resonance coefficients
Fully homogenized continuum	A_ξ to H_ξ , with index $\xi = \{\pi, \sigma, \epsilon, U\}$	None
Homogenized Biot continuum	$\mathbf{A}_\pi, \mathbf{H}_\pi, {}^4\mathbf{F}_\sigma, \mathbf{G}_\sigma, \mathbf{B}_\epsilon, \mathbf{C}_\epsilon, \mathbf{A}_U, \mathbf{H}_U$, (51)	None
Fully homogenized enriched continuum	A_ξ to H_ξ , with index $\xi = \{\pi, \sigma, \epsilon, U\}$	$\vec{a}, \vec{b}, \vec{c}, \vec{d}, \vec{\alpha}, \vec{\beta}, \vec{\gamma}, \vec{\delta}$, (52)
Homogenized enriched Biot continuum	$\mathbf{A}_\pi, \mathbf{H}_\pi, {}^4\mathbf{F}_\sigma, \mathbf{G}_\sigma, \mathbf{B}_\epsilon, \mathbf{C}_\epsilon, \mathbf{A}_U, \mathbf{H}_U$, (51)	$\vec{a}, \vec{\alpha}$

Note: The dispersion curves of each continuum type are shown in Figure D1.

In Figure 4B, the dispersion curve of the direct numerical simulation is compared with the enriched continua. The reference curves computed via the Bloch analysis (DNS), plotted with black crosses (+), are captured very well by the dispersion curves of the enriched continua computed with Equation (C1), including the three local resonant modes. The solid red line (—) shows the solution of the eigenvalue problem (C1) including all longwave and all local resonance coefficients whereas the dashed-blue line (---) includes only the Biot coefficients (51) and the local resonance coefficients (\vec{a} , $\vec{\alpha}$), see Table D1 that specifies the constitutive model used for each case. It demonstrates numerically that for the considered case, effectively, the constitutive response behaves as a homogenized enriched Biot continuum which is verified in Section 4.4.